https://doi.org/10.5194/wes-2026-209
Preprint. Discussion started: 17 November 2026
© Author(s) 2026. CC BY 4.0 License.

eawe european academy of wind energy
Open Access WIND ENERGY SCIENCE DISCUSSIONS

A dynamic engineering wake model for wind turbines under helix control

Tim Dammann[1], Wei Yu[2], and Jan-Willem van Wingerden[1]

[1]Delft Center for Systems and Control, Faculty of Mechanical Engineering, Delft University of Tehnology, Delft, The Netherlands
[2]Wind Energy Section, Department of Flow Physics and Technology, Faculty of Aerospace Engineering, Kluyverweg 1, 2629 HS Delft, Zuid-Holland, Netherlands

Correspondence: Tim Dammann (t.dammann@tudelft.nl)

Abstract. As wind farms increase in size and density, wake interactions between turbines reduce total energy capture and raise structural loads. Wind farm control strategies have therefore become essential for mitigating these effects. The helix wake-mixing strategy uses individual pitch control to impose a slowly rotating tilt–yaw moment on the rotor, deforming the wake into a helix and accelerating its recovery. Its power gains have been shown in large-eddy simulations (LES) and wind-tunnel experiments, yet existing engineering models capture only the time-averaged deficit of this intrinsically dynamic wake. This paper presents the first dynamic engineering model of the helix wake: a phase-locked, three-dimensional representation that rotates about the wake axis, enabling dynamic model-based wind farm control and helix-phase estimation. Derived from actuator-line LES of the IEA 22 MW reference wind turbine, it reconstructs the phase-resolved wake from only the actuation amplitude, frequency, and phase, and is validated on unseen test cases. Integrated into the dynamic wind farm framework OFF, the model is applied to a three-turbine row transitioning from free-stream to full wake alignment. With helix actuation on the first two turbines, the framework captures each helix wake arriving downstream only after its convection time and predicts the time-varying downstream power gain and incoming helix phase, about 190 times faster than real time.

1 Introduction

Wake interaction is one of the dominant loss mechanisms in wind farms.Turbines operating in the wake of upstream machines experience reduced wind speeds and increased turbulence, causing annual energy losses of 10–20% in typical offshore layouts together with elevated fatigue loading Barthelmie et al. (2009); Porté-Agel et al. (2020). The fluid mechanics of wind-turbine wakes and their interaction with the atmospheric boundary layer have been reviewed extensively Vermeer et al. (2003); Stevens and Meneveau (2017); Porté-Agel et al. (2020), and a broad hierarchy of wake models has been developed to predict these losses, ranging from analytical momentum-based models Jensen (1983); Katić et al. (1986); Bastankhah and Porté-Agel (2014); Niayifar and Porté-Agel (2016) and parabolic eddy-viscosity formulations Ainslie (1988) to large-eddy simulations (LES) Crespo et al. (1999); Sanderse et al. (2011); Göçmen et al. (2016).

Beyond passive layout optimization, *wind-farm flow control* actively manipulates the flow field to mitigate wake losses at the farm level Meyers et al. (2022); Houck (2022). The most mature strategy, wake steering, redirects the wake laterally

https://doi.org/10.5194/wes-2026-209
Preprint. Discussion started: 17 November 2026
© Author(s) 2026. CC BY 4.0 License.



eawe european academy of wind energy
Open Access WIND ENERGY SCIENCE DISCUSSIONS

by intentional yaw misalignment Bastankhah and Porté-Agel (2016); Gebraad et al. (2016); Howland et al. (2019) and has been demonstrated in field campaigns Fleming et al. (2019) and closed-loop implementations Doekemeijer et al. (2020). A second family of strategies, collectively referred to as *wake mixing*, does not displace the wake but accelerates its recovery by exciting large-scale coherent structures that enhance the entrainment of ambient momentum. Such forcing accelerates the intrinsic instabilities of turbine wakes. The near-wake tip-vortex system responds strongly to controlled perturbation Okulov and Sørensen (2007); Ivanell et al. (2010); Lignarolo et al. (2015), and the far wake naturally meanders at Strouhal numbers of 0.2–0.3 Medici and Alfredsson (2006); Larsen et al. (2008); Mao and Sørensen (2018), which explains why periodic forcing is most effective in precisely this band. Optimal-control studies of wind-farm boundary layers first revealed the potential of dynamic induction variations Goit and Meyers (2015); Munters and Meyers (2017), which were subsequently refined into the sinusoidal thrust modulation known as the pulse, with an optimal excitation frequency corresponding to a Strouhal number $\mathrm{St} = fD/U_\infty \approx 0.25$ Munters and Meyers (2018). The pulse has since been studied for turbine pairs Yılmaz and Meyers (2018), demonstrated in wind-tunnel experiments Frederik et al. (2020b); van der Hoek et al. (2022), and analyzed with respect to its load implications Frederik and van Wingerden (2022).

The *helix* approach of Frederik *et al.* Frederik et al. (2020a) extends this idea from axisymmetric thrust pulsing to a rotating, non-axisymmetric forcing. Using the multi-blade coordinate transformation familiar from individual pitch control for load mitigation Bossanyi (2003), low-frequency sinusoidal tilt- and yaw-moment perturbations are applied with a 90° phase offset, so that the induced thrust vector precesses slowly about the rotor axis. The wake deficit is deformed into a helical shape that breaks up significantly earlier than the unforced wake, yielding power gains for waked turbine pairs of up to 7.5% in LES Frederik et al. (2020a) while distributing the actuation more benignly over the pitch bearings than the pulse Frederik and van Wingerden (2022); van Vondelen et al. (2023a). Subsequent work has characterized the helix wake in detail: Korb *et al.* Korb et al. (2023) showed that the helical deflection is driven by the rotating in-plane forcing and identified a counter-rotating vortex pair (CVP) attached to the deflected wake, analogous to the CVP of the curled wake behind yawed turbines Martínez-Tossas et al. (2019); Howland et al. (2016), while Cheung *et al.* Cheung et al. (2024) analyzed the underlying fluid-dynamic mechanisms of Strouhal-timed actuation, and related work demonstrated wake-recovery enhancement through tip-vortex actuation Brown et al. (2022). Experimentally, the helix has been verified in wind-tunnel campaigns using tomographic PIV van der Hoek et al. (2024), and its interaction with realistic atmospheric conditions Taschner et al. (2023), floating platforms van den Berg et al. (2022, 2023), multi-turbine phase synchronization van Vondelen et al. (2023b) has been explored. High-fidelity studies of the helix increasingly rely on LES coupled to aeroelastic turbine models Taschner et al. (2024).

For wind-farm control synthesis, layout studies, and real-time model-based operation, high-fidelity LES is orders of magnitude too expensive; the field therefore relies on fast engineering wake models Meyers et al. (2022). Steady-state Gaussian wake models Bastankhah and Porté-Agel (2014); Ishihara and Qian (2018); Niayifar and Porté-Agel (2016) underlie widely used farm-level tools, and have been extended with double-Gaussian profiles that resolve the annular (ring-shaped) deficit of the near wake Keane et al. (2016); Keane (2021); Schreiber et al. (2020); Qian and Ishihara (2025), as well as with vortex-based descriptions of the curled wake behind yawed rotors Martínez-Tossas et al. (2019); Shapiro et al. (2018); Zong and Porté-Agel (2020); Bastankhah et al. (2022). Dynamic extensions such as FLORIDyn Gebraad and van Wingerden (2014); Becker et al.

https://doi.org/10.5194/wes-2026-209
Preprint. Discussion started: 17 November 2026
© Author(s) 2026. CC BY 4.0 License.



eawe european academy of wind energy
Open Access WIND ENERGY SCIENCE DISCUSSIONS

(2022) and related control-oriented flow models Lejeune et al. (2022); Becker et al. (2024) propagate wake properties downstream with the flow, enabling closed-loop farm control under time-varying conditions. Modeling efforts directed specifically at the helix have followed three routes. Data-driven reduced-order models based on dynamic mode decomposition Muscari et al. (2022); Gutknecht et al. (2023) reproduce the dominant helical modes but remain tied to the flow field on which they were trained. Free-vortex-wake methods van den Broek et al. (2022) resolve the relevant physics from first principles but are still too expensive for real-time farm-level application, while vortex-based engineering models reconstruct the helical deformation kinematically by displacing the wake with a discrete vortex system Gutknecht et al. (2026), at far lower cost but without a closed-form mapping from the control inputs to the deficit field. Steady-state engineering models for the helix Dammann et al. (2025, 2026a) do provide such a parametric deficit description, and have been used to quantify farm-level power gains, but they represent only the time-averaged wake and therefore discard the actuation phase entirely. However, the helix wake is an intrinsically dynamic phenomenon and requires

What is missing is a phase-resolved parametric engineering model, in the spirit of the Gaussian wake-model family, that maps the helix control inputs (pitch amplitude, actuation frequency, actuation phase) directly onto the evolving three-dimensional deficit field, and so exposes the instantaneous wake position and phase that a downstream rotor actually encounters. This helps to accurately predict time-depended power estimations considering varying ambient conditions and allowing for dynamic setpoint optimization for the helix approach in wind farms.

This paper develops and calibrates such a dynamic engineering model of the helix wake. The model is derived from a series of phase-averaged actuator-line LES of the IEA 22 MW reference wind turbine Zahle et al. (2024) spanning pitch amplitudes $\beta \in \{1,3,5\}^\circ$ and Strouhal numbers $\mathrm{St} \in \{0.25,0.28,0.30\}$. The main contributions are: (i) The development of the first dynamic engineering wake model which can provide the three dimensional instantaneous velocity field behind a turbine rotor as a function of actuation amplitude and frequency, time, and phase; (ii) the validation of the model based unseen LES data; (iii) the integration of the model into the dynamic wind farm flow control framework *OFF* and its demonstration on a three turbine wind farm considering changes in wind direction.

The remainder of the paper is organized as follows. Section 2 describes the LES setup, the helix implementation, and the post-processing procedure. Section 3 develops the wake model: the cross-plane structure (Sec. 3.1), the per-plane calibration (Sec. 3.2), the streamwise parameter functions (Sec. 3.3), and the amplitude and frequency scaling (Sec. 3.4). Section 4 validates the model against two LES cases held out from the calibration, and Section 5 demonstrates its use in the dynamic wind-farm simulation framework OFF Becker et al. (2024). Conclusions are drawn in Section 6.

2 Large-eddy simulation setup

2.1 Flow solver and numerical configuration

The wake data underlying the model are generated with the incompressible flow solver AMR-Wind Sprague et al. (2020); Sharma et al. (2024), a block-structured, adaptive-mesh LES code developed within the ExaWind ecosystem. The filtered Navier–Stokes equations are advanced with a Godunov-type finite-volume scheme with WENO-Z reconstruction and a fixed

https://doi.org/10.5194/wes-2026-209
Preprint. Discussion started: 17 November 2026
© Author(s) 2026. CC BY 4.0 License.

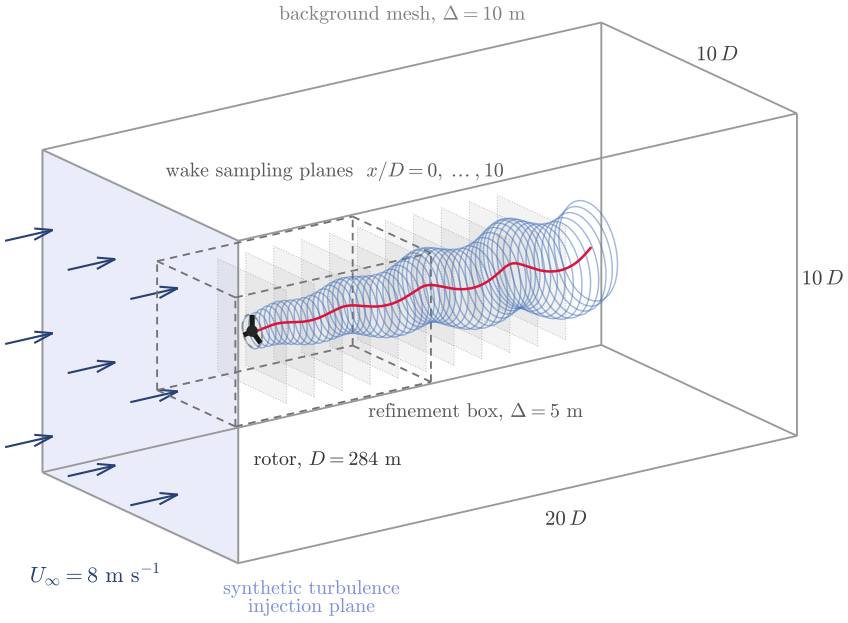


Figure 1. Computational domain, $20D \times 10D \times 10D$, with the rotor of diameter $D = 284\,\mathrm{m}$ located $4D$ from the inflow plane on the domain centerline. The dashed box marks the static mesh-refinement region ($\Delta = 5\,\mathrm{m}$); the background mesh spacing is $10\,\mathrm{m}$. Synthetic turbulence is injected through a forcing plane near the inlet. Dotted squares are the wake sampling planes.

time step of $\Delta t = 0.05\,\mathrm{s}$. Subgrid-scale stresses are closed with the standard Smagorinsky model Smagorinsky (1963). The molecular viscosity is $\mu = 1.8375 \times 10^{-5}\,\mathrm{kg\,m^{-1}\,s^{-1}}$ and the air density $\rho = 1.225\,\mathrm{kg\,m^{-3}}$.

The computational domain, sketched in Fig. 1, measures $20D \times 10D \times 10D$ and is discretized with a background mesh of $568 \times 284 \times 284$ cells ($\Delta = 10\,\mathrm{m}$). One static refinement level halves the mesh spacing to $\Delta = 5\,\mathrm{m}$ (57 cells per diameter) in a box extending from $2D$ upstream to $5D$ downstream of the rotor and $\pm 2D$ laterally and vertically, covering the rotor and the near wake where the helix structure is formed. Since the model targets the isolated actuation, an idealized inflow is used. A uniform free-stream velocity of $U_\infty = 8\,\mathrm{m\,s^{-1}}$ enters through a mass-inflow boundary and leaves through a pressure-outflow boundary, with slip conditions on all lateral boundaries. There is no ground plane, mean shear, or Coriolis force; the domain is centered on the hub, so the wake evolves in a symmetric environment analogous to uniform-inflow actuator-line studies Troldborg et al. (2010). Ambient turbulence is provided by a divergence-free synthetic turbulence field generated with TurbSim Jonkman (2009) on a $2800 \times 2800\,\mathrm{m}$ grid (nominal turbulence intensity 12%, Kaimal spectrum) and injected through

https://doi.org/10.5194/wes-2026-209
Preprint. Discussion started: 17 November 2026
© Author(s) 2026. CC BY 4.0 License.



eawe european academy of wind energy
Open Access WIND ENERGY SCIENCE DISCUSSIONS

a momentum-forcing plane as body forces near the inlet with a Gaussian smearing length of 120 m; the smearing acts as a low-pass filter, so the effective ambient turbulence intensity at the rotor is $I_a = 2.0\,\%$.

2.2 Turbine model and helix actuation

All simulations were conducted with the IEA 22 MW offshore reference wind turbine (RWT) Zahle et al. (2024) in its monopile configuration, with rotor diameter $D = 284\,\mathrm{m}$ and hub height 170 m. The turbine is represented by an actuator-line model (ALM) Sørensen and Shen (2002) coupled to the aero-servo-elastic solver OpenFAST National Renewable Energy Laboratory (2024), following the TurbineFastLine coupling in AMR-Wind Sharma et al. (2024); Churchfield et al. (2012). Each blade is discretized with 59 actuator points. The body force is projected onto the LES mesh with a Gaussian kernel of width $\varepsilon = 2\,\Delta_l$ (with Δ_l the local mesh size), in line with established smearing guidelines Martínez-Tossas et al. (2017).

The turbine operates in below-rated conditions at $U_\infty = 8\,\mathrm{m\,s^{-1}}$ under the ROSCO reference controller Abbas et al. (2022), which provides standard variable-speed torque control and, through its active wake control (AWC) module, the helix actuation. The helix is implemented with the inverse multi-blade-coordinate (Coleman) method (ROSCO `AWC_Mode` 2) Frederik et al. (2020a); Abbas et al. (2022). Sinusoidal pitch perturbations of amplitude β are applied in the non-rotating tilt–yaw frame at azimuthal mode number $n = +1$ and forcing frequency f_e, and transformed to individual blade-pitch commands. The resulting thrust-vector precession deflects the wake into a helix rotating at f_e. The forcing frequency is expressed as the Strouhal number $\mathrm{St} = f_e D/U_\infty$; for example, $\mathrm{St} = 0.28$ corresponds to $f_e = 7.887 \times 10^{-3}$ Hz, i.e. a helix period of $T_e \approx 127$ s. The unactuated thrust coefficient at this operating point is $C_T = 0.87$. The helix actuation reduces the mean thrust slightly, which is accounted for in the model calibration (Sec. 3.2).

2.3 Simulation matrix

Eight cases (about 40000 CPU hours each) are simulated (Table 1). Six are used for calibration: a greedy baseline, an amplitude series $\beta \in \{1, 3, 5\}^\circ$ at fixed $\mathrm{St} = 0.28$, and a frequency series $\mathrm{St} \in \{0.25, 0.30\}$ at fixed $\beta = 3^\circ$. The baseline serves both as the reference against which the helix gain is measured and as the $\beta = 0$ anchor of the amplitude scaling (Sec. 3.4). The remaining two simulations, at $\beta \in \{2, 4\}^\circ$ and $\mathrm{St} = 0.28$, are withheld from the calibration and interleaved with the amplitude series so that Sec. 4 can test interpolation on unseen data. This matrix covers the practically relevant helix operating envelope. Amplitudes above $\sim 5^\circ$ incur disproportionate pitch-actuator duty and thrust loss Frederik and van Wingerden (2022); van Vondelen et al. (2023a), while the mixing benefit peaks for $\mathrm{St} \approx 0.25$–0.30 Frederik et al. (2020a); Dammann et al. (2026b); Cheung et al. (2024). Each simulation covers 4310 s of physical time. One flow-through time (710 s) is discarded as spin-up, and the remaining 3600 s are used for data sampling, such that $N_e = 25$ complete helix cycles can be sampled depending on the actuation frequency.

https://doi.org/10.5194/wes-2026-209
Preprint. Discussion started: 17 November 2026
© Author(s) 2026. CC BY 4.0 License.



eawe european academy of wind energy
Open Access WIND ENERGY SCIENCE DISCUSSIONS

Table 1. Simulation matrix. All cases share $U_\infty = 8\,\mathrm{m\,s^{-1}}$, the domain of Fig. 1, and a sampling duration of 3600 s after one flow-through time. $T_e = 1/f_e$ is the helix period. Each case was sampled such that $N_e = 25$ complete helix cycles could be completed. C_T^{eff} is the amplitude-corrected thrust coefficient used in the model (Sec. 3.2). Case A0 is greedy (non-actuated) operation, treated throughout as $\beta = 0°$. The two cases below the rule, A2S28 and A4S28, are held out from every calibration stage and used only for the validation of Sec. 4.

	Case	β [°]	St	f_e [mHz]	t_{used} [s]	C_T^{eff}
Test cases	A0	0 (greedy)	—	—	—	0.870
	A1S28	1	0.28	7.887	3170	0.868
	A3S28	3	0.28	7.887	3170	0.858
	A5S28	5	0.28	7.887	3170	0.825
	A3S25	3	0.25	7.042	3550	0.858
	A3S30	3	0.30	8.451	2958	0.858
Validation cases	A2S28	2	0.28	7.887	3170	0.864
	A4S28	4	0.28	7.887	3170	0.846

2.4 Wake sampling and phase-averaged processing

Instantaneous velocity fields are stored at 1 Hz on 11 cross-stream (y–z) planes located at $x/D = k$, $k = 0, 1, \ldots, 10$, downstream of the rotor, each covering $10D \times 10D$ with 10 m resolution (280×280 points). One helix period is thus resolved by $T_e/1\,\mathrm{s} \gtrsim 118$ samples.

Because the helix forcing is periodic, the phase-locked mean wake is obtained by phase averaging. The sampling window is first trimmed to an integer number of 25 forcing periods, aligned such that averaging starts at zero actuation phase. Each snapshot is then assigned the phase $\varphi = 2\pi f_e t \bmod 2\pi$ and accumulated into 12 phase bins (30° per bin, $\gtrsim 250$ samples per bin and plane).

The phase-averaged fields are converted to velocity-deficit fields $\Delta u/U_\infty = (U_\infty - \bar{u})/U_\infty$ and condensed further by exploiting the rotational symmetry of the helix. In uniform, statistically axisymmetric inflow, advancing the actuation phase by $\Delta\varphi$ rotates the entire phase-locked wake pattern by $\Delta\varphi$ about the rotor axis. Each of the 12 phase-bin fields is therefore derotated by its bin phase and the results are averaged, yielding a single composite deficit field per downstream plane. This results in a twelvefold increase in effective sample count. Figure 2 illustrates the procedure for three of the twelve phases. These composite fields at $k = 0, \ldots, 10$ constitute the calibration data set for the wake model, where $k = x/D$ denotes the downstream distance. The model then reconstructs any actuation phase by rotating the composite pattern back (Sec. 3.1).

3 Model development

The model describes the phase-resolved deficit field $\Delta u(y, z, x, t)/U_\infty$ behind a helix-actuated rotor as a function of three control inputs: the pitch amplitude β, the Strouhal number St, and the actuation phase φ_0. It is constructed in three stages,

https://doi.org/10.5194/wes-2026-209
Preprint. Discussion started: 17 November 2026
© Author(s) 2026. CC BY 4.0 License.

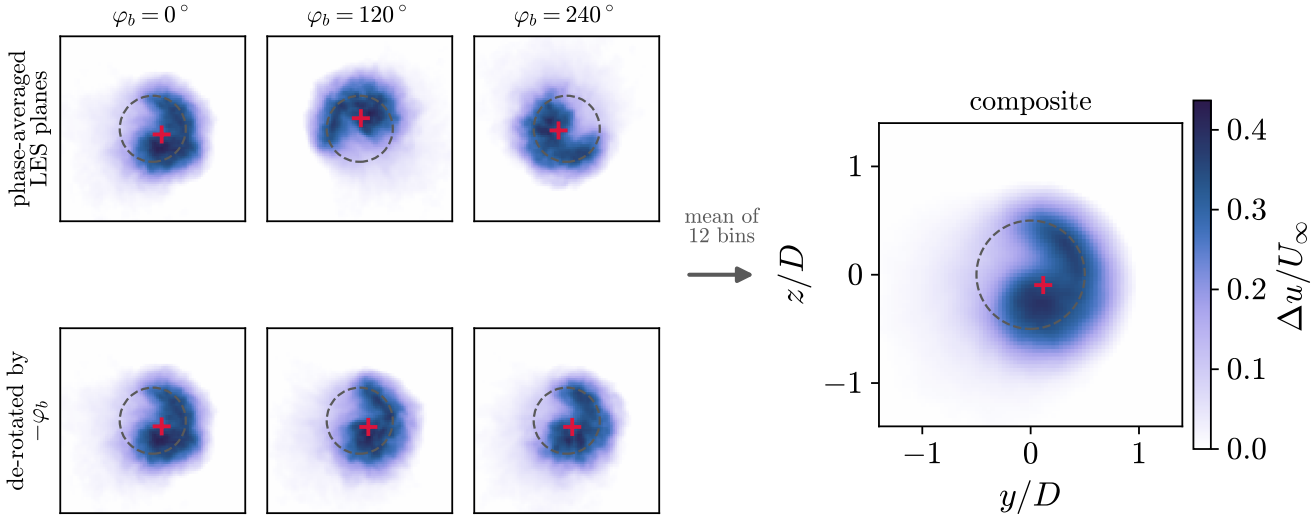


Figure 2. Construction of the composite calibration field, for case A5S028 at $x/D = 4$. Top: phase-averaged LES deficit planes for three of the twelve phase bins; the pattern rotates rigidly with the actuation phase φ_b. Bottom: the same planes de-rotated by $-\varphi_b$, which brings them into a common frame. Right: the mean over all twelve de-rotated bins, which constitutes the calibration data for that plane. Red crosses are the deficit-weighted centroids, the dashed circle is the rotor.

which mirror the following subsections: a parametric description of one wake cross-section (Sec. 3.1); the calibration of those parameters on each LES plane independently (Sec. 3.2); and the reduction of the per-plane parameters, first to smooth functions of the downstream distance (Sec. 3.3) and then to scaling relations in β and St (Sec. 3.4). Throughout, lengths are normalized by the rotor diameter D and velocities by U_∞.

3.1 Wake-plane structure

3.1.1 Helical centerline

Based on observations from the LES results, the wake centerline is described in each cross-plane by polar coordinates (r_h, φ_h) about the rotor axis,

$$y_c = r_h(k)\cos\varphi_h(k,t), \qquad z_c = r_h(k)\sin\varphi_h(k,t), \tag{1}$$

so that the locus of (y_c, z_c) over k traces the helix. The radius $r_h(k)$ grows monotonically from a small finite value at the rotor (the pitch excursion already displaces the thrust distribution in the plane where it acts, and the wake is deflected progressively thereafter) while the phase φ_h decreases linearly with k in the far wake and additionally rotates in time at the forcing frequency, $\partial\varphi_h/\partial t = \omega = 2\pi\,\mathrm{St}\,U_\infty/D$. The complete phase model, including a near-wake convection lag, is developed in Sec. 3.3.

https://doi.org/10.5194/wes-2026-209
Preprint. Discussion started: 17 November 2026
© Author(s) 2026. CC BY 4.0 License.

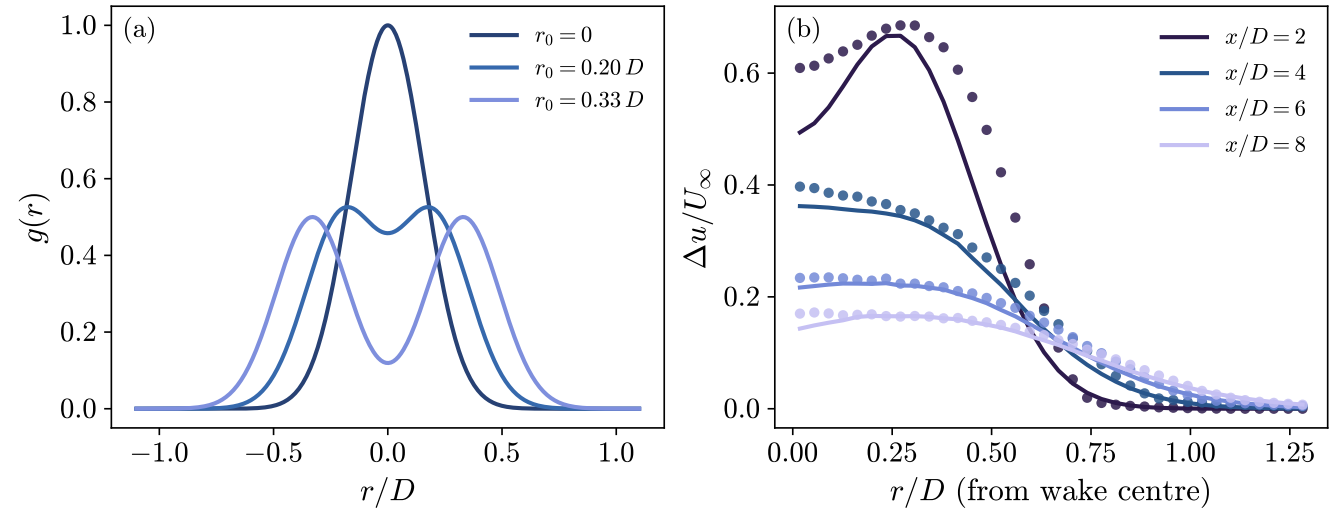


Figure 3. (a) Double-Gaussian ring profile [Eq. (3)] for increasing ring radius r_0 at fixed thickness σ; for $r_0 = 0$ the profile reduces exactly to a single Gaussian. (b) Azimuthally averaged LES deficit profiles for case A3S28 at several downstream planes (symbols) and the azimuthal averages of the corresponding fitted model fields (lines). The annular character of the deficit persists to the far wake: the profile remains flat-topped rather than collapsing to a single Gaussian.

3.1.2 Ring-shaped deficit profile

The velocity deficit in the plane is modeled as

$$\frac{\Delta u}{U_\infty}(y,z) = F\left(\sigma, r_0; C_T^{\text{eff}}\right)\, g(\tilde{r}), \tag{2}$$

where g is the double-Gaussian (ring) profile introduced for the near wake of unactuated turbines by Keane *et al.* Keane et al. (2016); Keane (2021) and Schreiber *et al.* Schreiber et al. (2020), and later adapted to describe the full wake of a wind turbine by Qian and Ishihara Qian and Ishihara (2025) and finally refined to also account for helix actuation by Dammann *et al.* Dammann et al. (2026a).

$$g(r) = \tfrac{1}{2}\left[e^{-(r-r_0)^2/2\sigma^2} + e^{-(r+r_0)^2/2\sigma^2}\right], \tag{3}$$

with ring radius r_0 and ring thickness σ [Fig. 3(a)]. For $r_0 = 0$, Eq. (3) reduces exactly to a single Gaussian. The time-averaged helix deficit remains distinctly annular over the entire observed range [Fig. 3(b)], because the rotating deflection continuously re-displaces the deficit off the centerline, and the composite (co-rotating-frame) field aggregates a hub-jet-dominated core with an off-axis deficit maximum.

https://doi.org/10.5194/wes-2026-209
Preprint. Discussion started: 17 November 2026
© Author(s) 2026. CC BY 4.0 License.



eawe european academy of wind energy
Open Access WIND ENERGY SCIENCE DISCUSSIONS

3.1.3 Momentum-based amplitude

The amplitude F in Eq. (2) is determined from integral streamwise momentum conservation, in the spirit of self-similar wake theory Bastankhah and Porté-Agel (2014); Shapiro et al. (2018). Following Qian and Ishihara Qian and Ishihara (2025), the amplitude is evaluated by the third-order expansion of the analytical solution, originally derived by Keane *et al.* Keane et al. (2016); Keane (2021) and Schreiber *et al.* Schreiber et al. (2020).

$$F = \frac{C_T^{\mathrm{eff}}}{8M} + \frac{N\left(C_T^{\mathrm{eff}}\right)^2}{64\,M^3} + \frac{N^2\left(C_T^{\mathrm{eff}}\right)^3}{128\,M^5}, \tag{4}$$

with:

$$M = 2\sigma^2 e^{-\frac{r_0^2}{2\sigma^2}} + \sqrt{2\pi} r_0 \sigma\,\mathrm{erf}\left(\frac{r_0}{\sqrt{2}\sigma}\right) \quad \text{and} \quad N = \sigma^2 e^{-\frac{r_0^2}{\sigma^2}} + \frac{\sqrt{\pi}}{2} r_0 \sigma\,\mathrm{erf}\left(\frac{r_0}{\sigma}\right). \tag{5}$$

This expression avoids unphysical solutions in the near-wake and ensures a smooth trend which is consistent with observations from the LES.

The effective thrust coefficient accounts for the mean thrust loss of the helix actuation, which grows with pitch amplitude. From the turbine response, this loss is captured by a cubic polynomial

$$C_T^{\mathrm{eff}}(\beta) = C_T\,\eta(\beta), \qquad \eta(\beta) = 1 - 3.233\times10^{-3}\beta + 9.575\times10^{-4}\beta^2 - 4.731\times10^{-4}\beta^3 \tag{6}$$

with β in degrees and $C_T = 0.87$ the unactuated thrust coefficient at the operating point (Table 1).

3.1.4 Counter-rotating vortex pair

Following the observation that the deflected helix wake carries an attached CVP Korb et al. (2023), analogous to the curled wake of yawed rotors Martínez-Tossas et al. (2019); Howland et al. (2016); Bastankhah et al. (2022); Zong and Porté-Agel (2020), the radial coordinate in Eq. (2) is evaluated after a vortex-induced displacement. Two Lamb–Oseen vortices of circulation $\pm\Gamma$ and core radius r_c are placed at $(y_c, z_c) \pm d_v\,\boldsymbol{e}_\perp$, where $\boldsymbol{e}_\perp$ is the unit vector perpendicular to the instantaneous displacement direction φ_h and $d_v = 0.05$ is fixed as no choice of $d_v > 0$ changes the reconstructed field since only $\Gamma \cdot d_v$ is identifiable. Each vortex induces the tangential velocity

$$v_\theta(\varrho) = \frac{\Gamma}{2\pi\varrho}\left(1 - e^{-\varrho^2/r_c^2}\right), \tag{7}$$

where ϱ is the distance to the vortex center. The combined induced field $\boldsymbol{v}$ of the pair deforms the deficit pattern. The ring profile is then evaluated at the displaced coordinate

$$(\tilde{y}, \tilde{z}) = (y', z') - \boldsymbol{v}(y', z'), \qquad \tilde{r} = \sqrt{\tilde{y}^2 + \tilde{z}^2}, \tag{8}$$

where (y', z') are coordinates relative to the wake center. The sampling point is traced to where the fluid came from, and the effective exposure time of a wake element to the crossflow is absorbed into the calibrated circulation $\Gamma(k)$, so that $\boldsymbol{v}$ carries units of length. A sketch of the CVP geometry can be seen in 4. Deforming a mean wake profile with a Lamb–Oseen crossflow,

https://doi.org/10.5194/wes-2026-209
Preprint. Discussion started: 17 November 2026
© Author(s) 2026. CC BY 4.0 License.

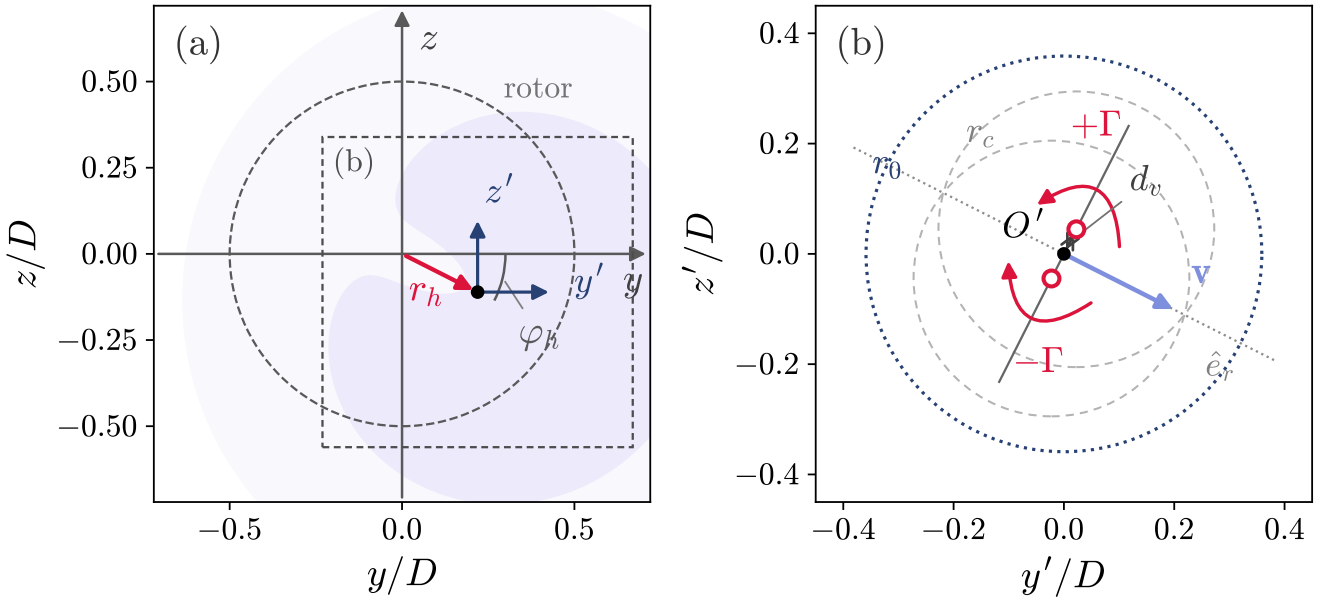


Figure 4. Geometry of the CVP, drawn from the calibrated parameters of case A5S28 at $x/D = 7$. (a) Global frame (y, z) centered on the rotor axis; the wake center O' is located by the helix radius r_h and phase φ_h [Eq. (1)], and the wake-centered frame (y', z') is a pure translation of the global one. The dashed box marks the detail shown in (b). (b) The two Lamb–Oseen cores sit at $\pm d_v$ along the direction perpendicular to the radial unit vector $\hat{e}_r$, carrying circulations $+\Gamma$ (counter-clockwise) and $-\Gamma$; grey dashed circles indicate the core radius r_c and the blue dotted circle the deficit-ring radius r_0. Their combined induced field displaces the wake center radially outward by $\boldsymbol{v}$, Eq. (8).

underlies curled-wake models for yawed rotors Martínez-Tossas et al. (2019); Shapiro et al. (2018) and the vortex-based helix wake model of Gutknecht *et al.* Gutknecht et al. (2026). The latter applies the displacement as a finite rotation about each vortex core while we retain the linear form. The CVP strength $\Gamma(k)$ is calibrated per plane, while the core radius r_c is held at a single global constant (Sec. 3.2).

3.2 Per-plane calibration

The parameters $\boldsymbol{p}(k)$ are calibrated independently on each composite deficit plane $k = 0, \ldots, 10$ for each case. The centerline (r_h, φ_h) is taken directly from the deficit-weighted centroid of the LES plane (momentum centroid, evaluated on the mask $\Delta u/U_\infty > 0.05$), as freeing the centerline would let it compete with the CVP circulation Γ for the same asymmetry in the residual.

The CVP core radius is not fitted either but pinned globally to

$$r_c = 0.25\, D, \tag{9}$$

https://doi.org/10.5194/wes-2026-209
Preprint. Discussion started: 17 November 2026
© Author(s) 2026. CC BY 4.0 License.

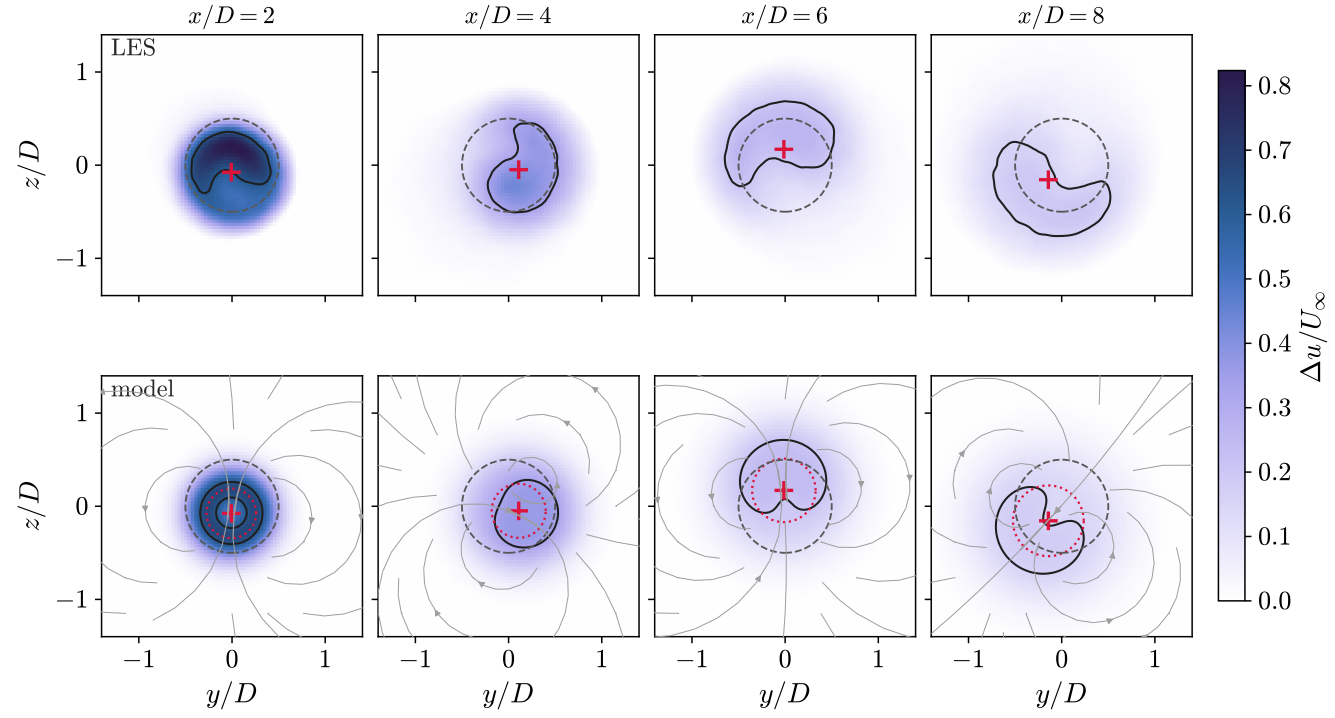


Figure 5. Phase-locked deficit fields for case A3S28 ($\beta = 3°$, St $= 0.28$): LES composite (top row) and calibrated model (bottom row) at $x/D = 2, 4, 6, 8$. The red cross marks the modeled wake centerline, the dotted circle the ring radius r_0, and the grey dashed circle the rotor. The grey streamlines indicate the displacement through the CVP. The black iso-deficit contours show 75% of the peak deficit.

the median of the freely fitted per-plane values over the model's validity range across all six cases. The reconstructed field turns out to be almost insensitive to r_c. Pinning it therefore removes three weakly identified coefficients from the amplitude scaling.

The remaining three parameters (σ, r_0, Γ) are fitted by minimizing a weighted root-mean-square residual between Eq. (2) and the LES deficit, with weights that emphasize the wake region (double weight where $\Delta u/U_\infty > 0.05$, one-tenth weight beyond $r > 1.2$ from the axis). A differential-evolution global search followed by a limited memory Broyden–Fletcher–Goldfarb–Shanno algorithm polish is used on every plane, with the search box progressively tightened around the previous plane's solution; F is recomputed from Eq. (4) inside the loop, so the amplitude closure is enforced exactly at every iteration.

In the first two planes, the fit trades an artificially small σ against an inflated r_0. These two planes are therefore excluded when the streamwise function for r_0 is fitted (Sec. 3.3).

Figure 5 compares LES and calibrated model planes for the $\beta = 3°$ case. The model captures the off-axis deficit, the annular shape, the CVP-induced asymmetry, and the amplitude decay. Quantitative agreement is reported in Sec. 4, on cases withheld from the calibration.

https://doi.org/10.5194/wes-2026-209
Preprint. Discussion started: 17 November 2026
© Author(s) 2026. CC BY 4.0 License.



eawe european academy of wind energy
Open Access WIND ENERGY SCIENCE DISCUSSIONS

Table 2. Streamwise parameter functions of the model. Each parameter of the wake-plane description (Sec. 3.1) is a smooth function of the downstream distance $k = x/D$, fitted to the per-plane calibration values. Together the model has 12 coefficients per operating point (φ_0 is a control input; the lag length $k_u = 2$, the CVP core radius r_c, the ring-thickness constants $a_0 = 0.080\,D$, $c_0 = 0.30$ and $k_\sigma = 0.70\,D$, and the ring-radius constants $a_0^r = 0.12\,D$, $c_0^r = 0.22$ and $k_s = 2.0\,D$ are global). "Planes" lists the planes entering each streamwise fit.

Parameter	Function	Coeff.	Planes	Role
$\sigma(k)$	$a_0 + \frac{b\,k}{\sqrt{1+c_0 k}} + c e^{-(k/k_\sigma)^2}$, Eq. (10)	2	all	ring thickness
$r_0(k)$	$a_0^r + \frac{b\,k}{\sqrt{1+c_0^r k}} + c e^{-(k/k_s)^2}$, Eq. (11)	2	$k \neq 1,2$	ring radius
$\Gamma(k)$	$L\,\frac{s(k)-s(0)}{1-s(0)}$, Eq. (12)	3	$k \geq 3$	CVP circulation
r_c	const $= 0.25\,D$	0	—	CVP core radius
$r_h(k)$	$c + a\,k$, Eq. (13)	2	all	helix radius
$\varphi_h(k)$	$\varphi_0 - k_x k - c(1 - e^{-k/k_u})$, Eq. (14)	3	all	helix phase

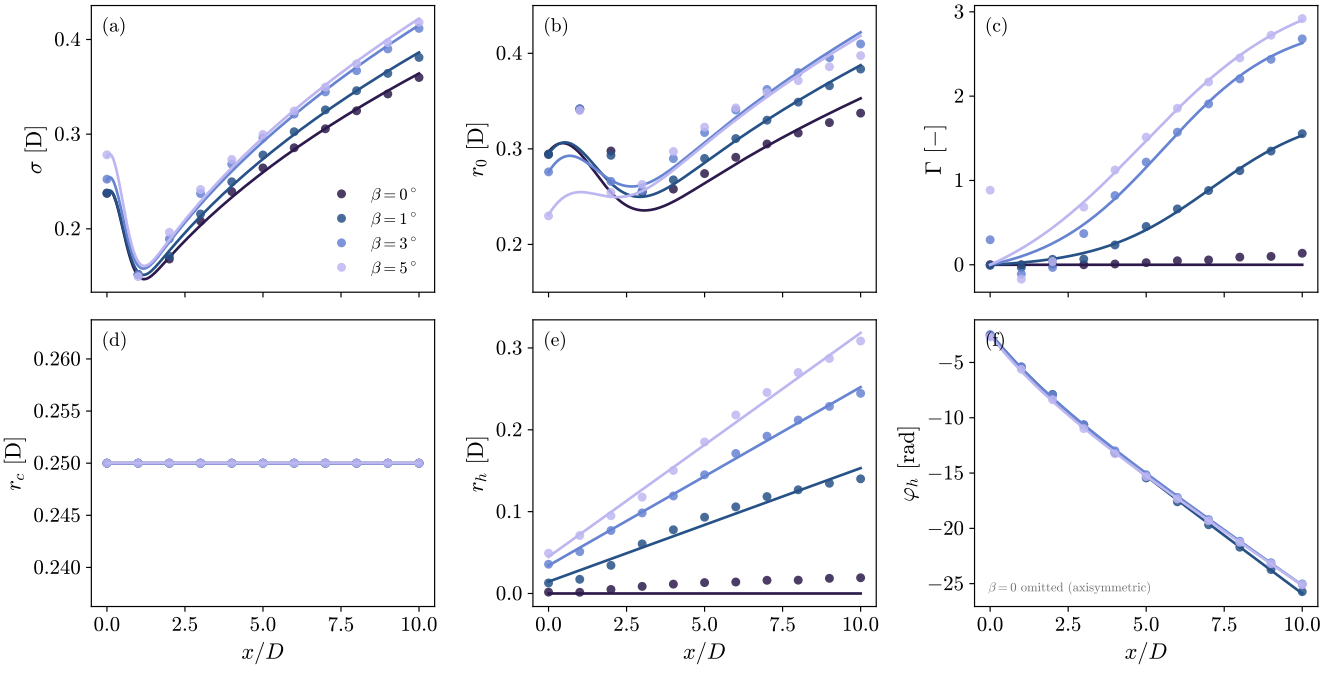


Figure 6. Streamwise evolution of the model parameters for the amplitude series (St = 0.28). Symbols: per-plane calibration values; lines: streamwise functions of Table 2. The helix phase φ_h is shown unwrapped; its slope sets the helix pitch and hence the implicit convection velocity U_c.

3.3 Streamwise parameter functions

The per-plane parameters are condensed into the smooth streamwise functions listed in Table 2 and shown in Fig. 6. Three modeling choices deserve discussion.

https://doi.org/10.5194/wes-2026-209
Preprint. Discussion started: 17 November 2026
© Author(s) 2026. CC BY 4.0 License.



eawe european academy of wind energy
Open Access WIND ENERGY SCIENCE DISCUSSIONS

3.3.1 Ring thickness

The ring thickness starts high at the rotor plane, collapses to a minimum $1\,D$ downstream, and grows steadily from there. The model represents this as a wake-width growth law plus a narrow near-wake bump:

$$\sigma(k) = a_0 + \frac{b\,k}{\sqrt{1 + c_0 k}} + c\,e^{-(k/k_\sigma)^2}, \qquad \begin{aligned} a_0 &= 0.08\,D, \\ c_0 &= 0.30, \\ k_\sigma &= 0.70\,D, \end{aligned} \tag{10}$$

with a_0, c_0 and k_σ global constants (obtained from fitting), so that only the growth rate b and the bump amplitude e are calibrated per case.

3.3.2 Ring radius

The ring radius uses the same structure as the ring thickness:

$$r_0(k) = a_0^r + \frac{b\,k}{\sqrt{1 + c_0^r k}} + c\,e^{-(k/k_s)^2}, \qquad \begin{aligned} a_0^r &= 0.12\,D, \\ c_0^r &= 0.22, \\ k_s &= 2.0\,D, \end{aligned} \tag{11}$$

with a_0^r, c_0^r and k_s global (obtained from fitting), so only (b, e) are calibrated per case.

3.3.3 CVP circulation

The circulation grows sigmoidally as the vortex system rolls up, anchored to vanish at the rotor plane:

$$\Gamma(k) = L\,\frac{s(k) - s(0)}{1 - s(0)}, \qquad s(k) = \frac{1}{1 + e^{-a(k - k_0)}}, \tag{12}$$

so that $\Gamma(0) = 0$ exactly and $\Gamma(k \to \infty) = L$, where k_0 is the location of the transition point of the sigmoid along the k-axis, and a controls how rapidly the sigmoid changes around k_0. A plain sigmoid only approaches zero asymptotically and therefore cannot vanish at the rotor, yet the vortex system needs 2–$4D$ to roll up Martínez-Tossas et al. (2019); Korb et al. (2023) and carries no circulation where it has not yet formed.

The near-wake planes ($k \leq 2$) are excluded from this fit as the CVP has not formed yet Korb et al. (2023) and the fitted values are therefore deemed fitting noise. Fitting Γ on $k \geq 3$ instead leaves all three coefficients well determined and monotone in amplitude, which makes their scaling relations usable (Sec. 3.4).

3.3.4 Near-rotor anchoring

Apart from Γ, the functions are fitted over the full range including the rotor plane, rather than over the far wake only. Extrapolating far-wake fits toward the rotor produces unphysical amplitude artifacts.

https://doi.org/10.5194/wes-2026-209
Preprint. Discussion started: 17 November 2026
© Author(s) 2026. CC BY 4.0 License.



eawe european academy of wind energy
Open Access WIND ENERGY SCIENCE DISCUSSIONS

3.3.5 Helix radius

The centerline radius grows linearly from a finite offset at the rotor,

$$r_h(k) = c + a\,k. \tag{13}$$

The phase-locked LES centroid is *already* displaced at the rotor plane, growing with amplitude, because the individual-pitch excursion acts on the blades themselves and the resulting thrust asymmetry is present in the plane where it is generated. Both coefficients grow with amplitude and are set to zero for the greedy baseline, which has no rotating thrust asymmetry and therefore no centerline displacement (Sec. 3.4).

3.3.6 Helix phase and convection velocity

The phase evolution is modeled as

$$\varphi_h(k,t) = \varphi_0 + \omega t - k_x\,k - c\left(1 - e^{-k/k_u}\right), \qquad \omega = 2\pi\,\mathrm{St}\,\frac{U_\infty}{D}, \tag{14}$$

fitted on the unwrapped per-plane centroid phases. Since the entire pattern rotates rigidly at ω, the phase at distance k equals the actuation phase φ_0 delayed by the travel time $\int_0^k \mathrm{d}k'/U_c(k')$ of the wake. Equation (14) therefore has an integrated-convection model. A uniform convection velocity would give a pure straight line $\varphi_h = \varphi_0 - k_x k$. The exponential term captures the slower convection in the near wake, where the deficit is strongest. The far-wake slope defines the centerline wavelength $\lambda = 2\pi/k_x$ and the asymptotic convection velocity

$$\frac{U_c}{U_\infty} = \frac{2\pi\,\mathrm{St}}{k_x}, \tag{15}$$

while the lag amplitude c measures the accumulated extra phase (about 0.3–0.5 helix turns at $\beta = 3°$) incurred before the wake reaches U_c. The development length is found to pin at $k_u = 2$ in every case when left free, and is therefore fixed globally. The greedy baseline is excluded here, as its wake is axisymmetric. The lag amplitude factorizes as $c = \mathrm{St}\,\tau$ with $\tau \approx (9.0 + 0.58\,\beta)\,D/U_\infty$: across the frequency series the lag collapses onto a Strouhal-independent time delay and it grows weakly with amplitude because stronger actuation deepens the near-wake deficit.

The complete streamwise description requires 12 coefficients per operating point (Table 2); Fig. 7 shows the resulting centerline against the LES centroids.

3.3.7 Validity range

The near-wake planes bound where the plane description is usable, and therefore fix the application range of the model. The per-plane reconstruction error is dominated by the first three planes. This, with the exclusion of $k \le 2$ from the r_0 fit discussed above, sets $k \ge 3$ ($x/D \ge 3$) as the validity range of the model; all quantitative results below are reported over it.

3.4 Amplitude and frequency scaling

The final reduction step turns the 12 per-case coefficients into functions of the control inputs.

https://doi.org/10.5194/wes-2026-209
Preprint. Discussion started: 17 November 2026
© Author(s) 2026. CC BY 4.0 License.

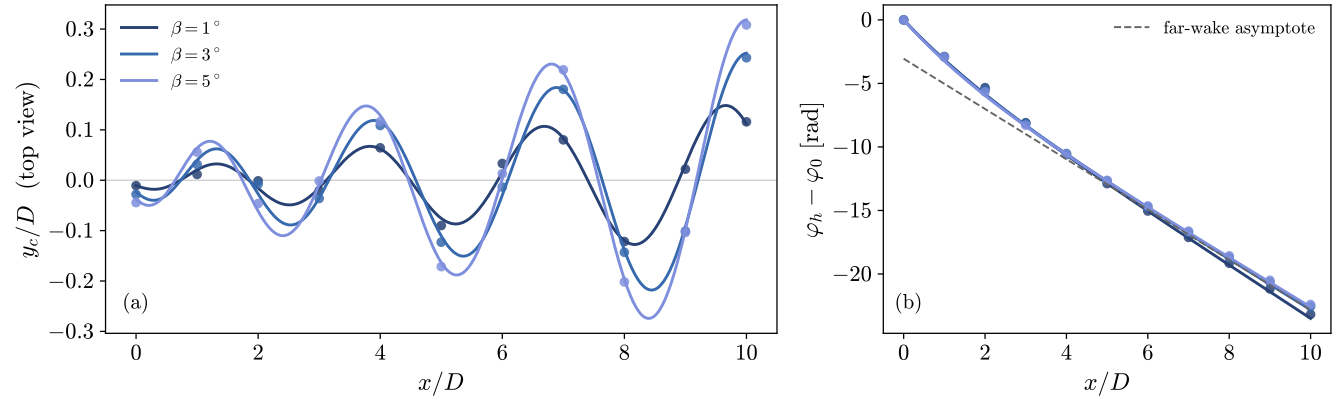


Figure 7. Helical wake centerline. (a) Top view of the modeled centerline [Eqs. (1) and (14)] and the per-plane LES centroids for the amplitude series. (b) Unwrapped centerline phase $\varphi_h(k)$: symbols, LES centroids; lines, Eq. (14). The slope of the far-wake asymptote (dashed) yields the convection velocity U_c; the offset accumulated in the near wake represents the Strouhal-independent time lag.

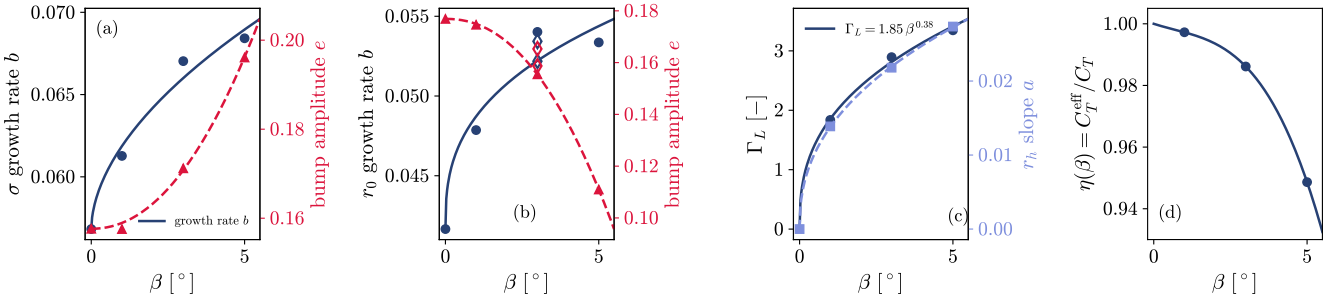


Figure 8. Scaling of curated streamwise-function coefficients with pitch amplitude β (symbols: calibrated cases at $\mathrm{St} = 0.28$; lines: scaling relations of Eq. (16); the $\beta = 0$ symbol is the greedy baseline, which the relations are anchored to). (a) ring-thickness coefficients of Eq. (10): growth rate b (left axis) and rotor-plane bump amplitude e (right axis); the offset a_0, transition c_0 and bump width k_σ are global constants and therefore have no scaling relations. (b) the same pair for the ring radius r_0 [Eq. (11)]: the growth rate steepens with amplitude while the rotor-plane bump decays. Open diamonds are the two St-series cases ($\mathrm{St} = 0.25$ and 0.30, both at $\beta = 3^\circ$), calibrated independently and falling within 6% of the amplitude relation. (c) CVP circulation amplitude $\Gamma_L \propto \beta^{0.38}$ and helix-radius slope a [Eq. (13)]; (d) thrust-loss factor $\eta(\beta)$ [Eq. (6)].

https://doi.org/10.5194/wes-2026-209
Preprint. Discussion started: 17 November 2026
© Author(s) 2026. CC BY 4.0 License.



eawe european academy of wind energy
Open Access WIND ENERGY SCIENCE DISCUSSIONS

3.4.1 Amplitude scaling

Every shape and centerline coefficient is expressed in the baseline-plus-contribution form

$$c(\beta) = c_{\text{base}} + c_1\,\beta^{c_2}, \tag{16}$$

in which c_{base} is *fixed* to the coefficient obtained from fitting the greedy baseline (case A0) and only (c_1, c_2) are fitted to the helix amplitude series. The same structure is used in the steady-state helix wake model of Dammann *et al.* Dammann et al. (2026a).

The CVP circulation and the wake deflection are the exception as both must vanish for an unactuated rotor, which has neither a CVP nor a rotating thrust asymmetry. They are therefore set to zero for the baseline rather than fitted, so that $c_{\text{base}} = 0$ and Eq. (16) reduces to a pure power law. This gives $\Gamma_L = 1.85\,\beta^{0.38}$ for the circulation and $a_{r_h} = 0.0138\,\beta^{0.42}$, $c_{r_h} = 0.0156\,\beta^{0.67}$ for the two centerline coefficients of Eq. (13).

Figure 8 collects the scaling relations, and Fig. 9 shows their combined effect on the reconstructed wake in the two longitudinal symmetry planes. With increasing amplitude the helix corridor widens, the deficit is shed laterally earlier, and the far-wake deficit is visibly weaker.

3.4.2 Strouhal transferability

We found that within the cases examined, ($\mathrm{St} = 0.25, 0.30$ at $\beta = 3°$) the Strouhal number does not alter the *shape* of the velocity deficit, but only (i) the rotation rate $\omega = 2\pi \mathrm{St} U_\infty / D$ and (ii) the centerline wavelength through Eq. (15) with U_c and the time lag τ unchanged.

Figure 10 visualizes that across the Strouhal series the reconstructed wake envelope, deficit magnitude, and centerline amplitude are indistinguishable, and only the centerline wavelength $\lambda = 2\pi/k_x = U_c/(\mathrm{St}\,U_\infty)\,D$ contracts from $3.5\,D$ at $\mathrm{St} = 0.25$ to $2.9\,D$ at $\mathrm{St} = 0.30$. However, we would like to note that this assumption might work in the tested Strouhal-range, but should not be extrapolated to actuation frequencies laying outside of it.

The assembled model thus maps $(\beta, \mathrm{St}, \varphi_0) \mapsto \Delta u(y, z, k, t)/U_\infty$ through: Eqs. (2)–(8) (deficit field), with time entering only through the rigid rotation ωt in Eq. (14) via the scaling relations of Fig. 8 (coefficients), and the streamwise functions of Table 2 (parameters at k). Evaluation of a full 280×280 plane takes milliseconds on a single core, compatible with real-time farm-model applications Becker et al. (2022, 2024).

Table 3 collects the complete calibration. Given the three control inputs $(\beta, \mathrm{St}, \varphi_0)$, the relations in the upper block return every streamwise-function coefficient, those functions return the five wake-plane parameters at any k, and Eqs. (2)–(8) return the deficit field.

4 Validation

This section validates the model using two unseen LES cases: $\beta = 2°$ and $4°$, both at $\mathrm{St} = 0.28$ (cases A2S28 and A4S28 of Table 1). They are deliberately placed between the calibration amplitudes 1, 3 and 5°, so they test interpolation of the amplitude

https://doi.org/10.5194/wes-2026-209
Preprint. Discussion started: 17 November 2026
© Author(s) 2026. CC BY 4.0 License.

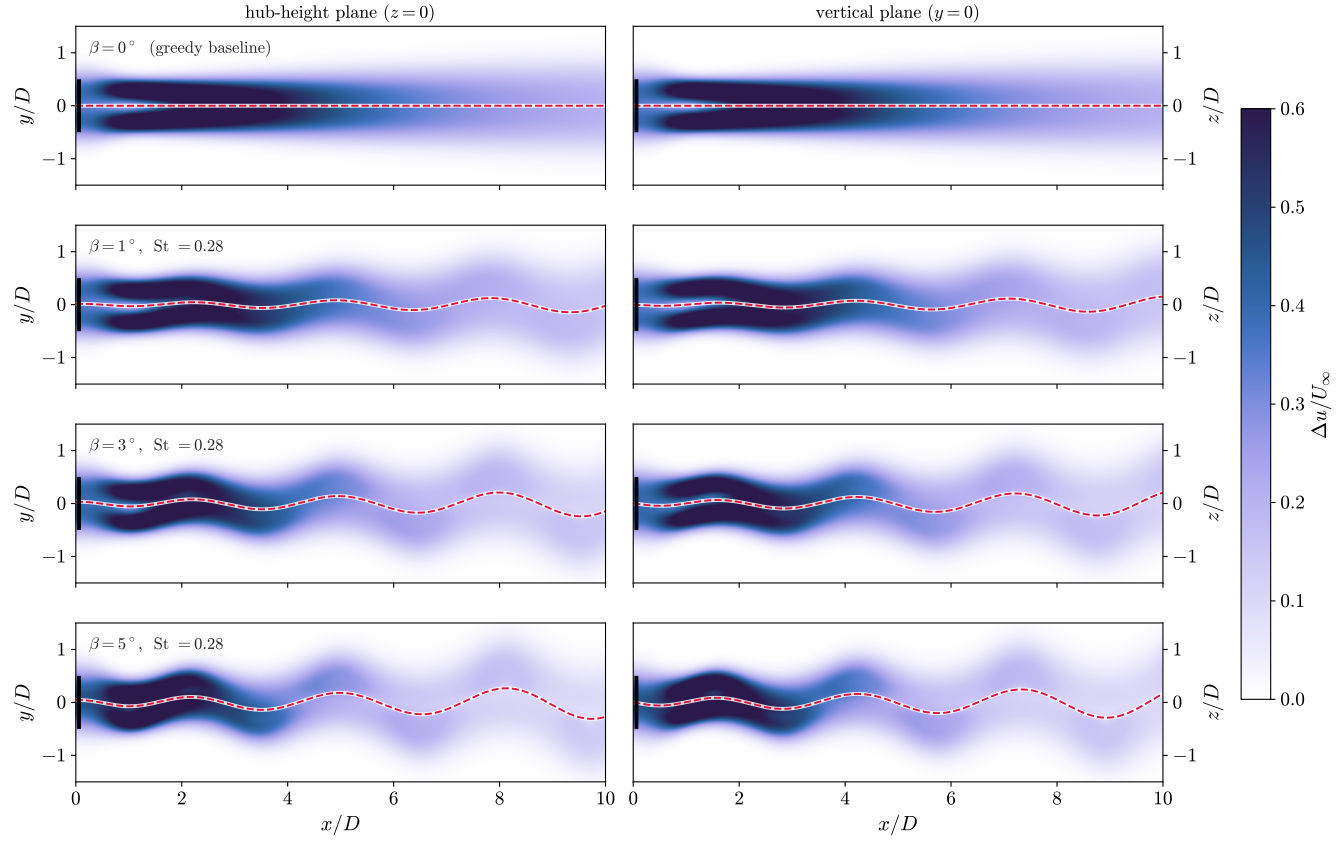


Figure 9. Reconstructed helix wake for the amplitude series ($\mathrm{St} = 0.28$, $\varphi_0 = 0$): velocity deficit at hub height (left column) and in the vertical symmetry plane (right column). The top row is the greedy baseline, which the same model reproduces at $\beta = 0$. The dashed line is the modeled helical centerline [Eqs. (1) and (14)]; the black bar marks the rotor.

scaling relations of Sec. 3.4, which is precisely the regime a farm controller sweeping a continuous set point operates in, and the regime in which the model would be used to decide an amplitude it has never seen.

Figure 11 shows the predicted fields against the LES. The annular deficit, its lateral displacement, and its azimuthal orientation are reproduced at every station. The visible discrepancy is a mild smoothing of the LES kidney shape, whose sharp inner edge the five-parameter plane description cannot resolve. Quantitatively, over the validity range $x/D = 3$–10 the model reaches a mean RMSE of 0.0271 at $\beta = 2°$ and 0.0309 at $4°$ on the validation wake mask ($\Delta u/U_\infty > 0.03$). For reference, re-predicting the six calibration cases with the same assembled model gives 0.026–0.033.

The engineering measures (Fig. 12) are reproduced more accurately than the pointwise RMSE alone would suggest. The rotor-averaged deficit is predicted to within 2.4% ($2°$) and 3.5% ($4°$) in the mean, with a continuos decay from $x/D = 3$ to 10. The RMSE consistently stays below a value of 0.05 throughout the validity range for both amplitudes. This is in line with

https://doi.org/10.5194/wes-2026-209
Preprint. Discussion started: 17 November 2026
© Author(s) 2026. CC BY 4.0 License.

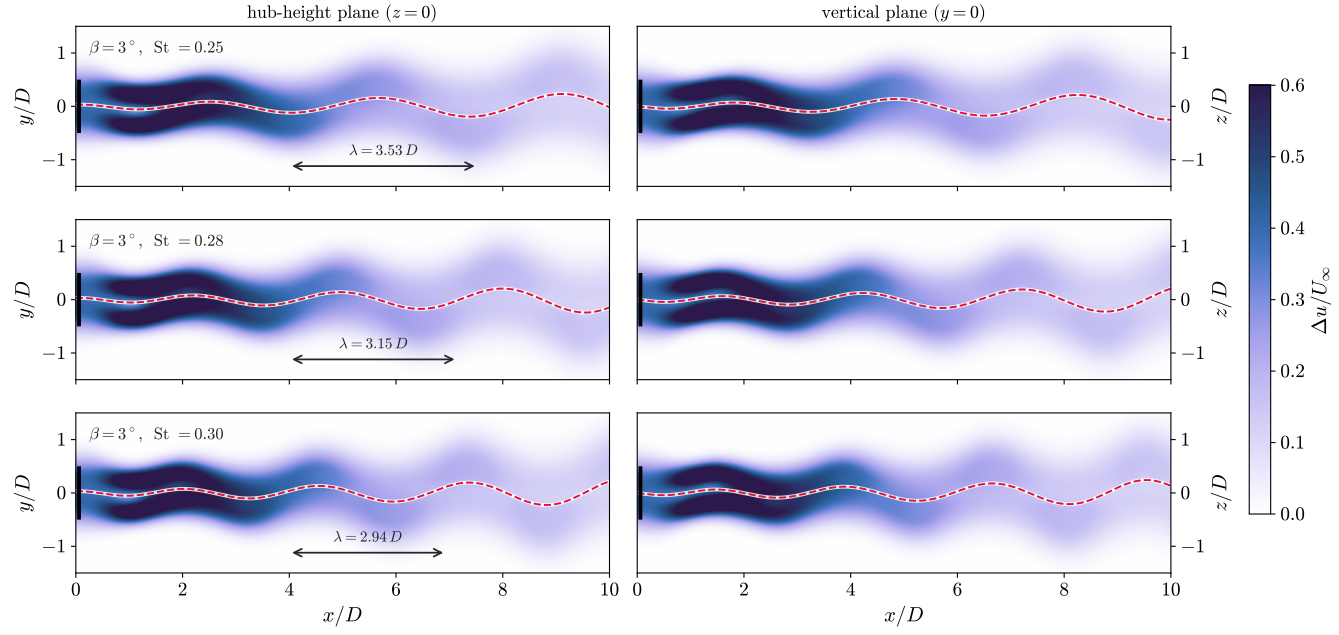


Figure 10. Reconstructed helix wake for the Strouhal series ($\beta = 3°$, $\varphi_0 = 0$), presented as in Fig. 9. The wake shape is Strouhal-independent: only the centerline wavelength $\lambda = 2\pi/k_x$ (arrows) changes, while deficit magnitude and centerline amplitude are unaffected.

the accuracy measured in state-of-the-art steady-state engineering wake models Ishihara and Qian (2018); Qian and Ishihara (2025); Dammann et al. (2026a).

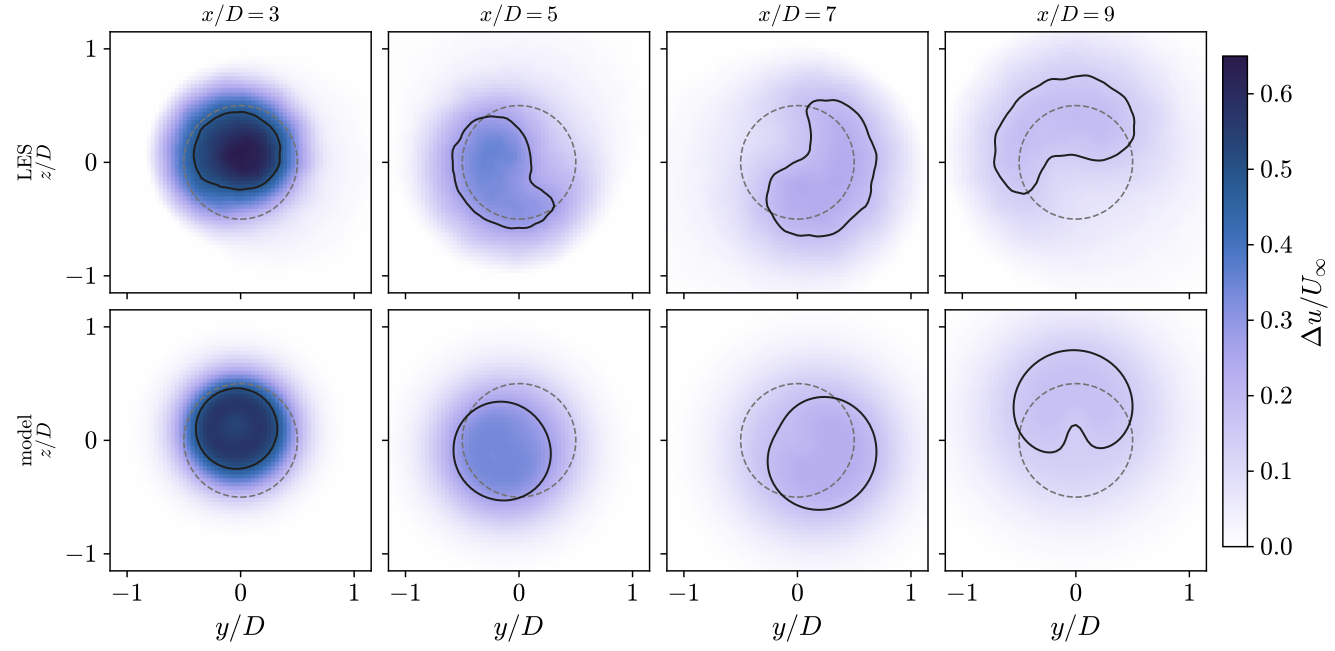
Figure 13 shows the validation of the modeled wake centerline. The left and middle panel show the top and side view of the wake respectively. The right panel shows the two centerlines as seen when looking from the rotor plane. Both cases track the LES closely and show a well reproduced overall magnitude. The modeled spiral follows the LES centroid in both longitudinal projections, with a mean in-plane offset of $0.019\,D$ (2°) and $0.016\,D$ (4°) over the validity range.

The offset is not uniform along the wake. It stays between 0.009 and $0.017\,D$ from $x/D = 3$ to 8 with no trend, then grows to $0.052\,D$ and $0.042\,D$ at $x/D = 10$. The phase error changes sign along the wake. The model leads the LES by up to 6° around $x/D = 5$ and lags it by 14° (2°) and 8° (4°) at $x/D = 10$. This is a mild misprediction of the local centerline wavelength rather than an accumulating drift. Since the helix radius is largest in the far wake, a given angular error there maps to the largest in-plane displacement, which is why the last two planes dominate the mean.

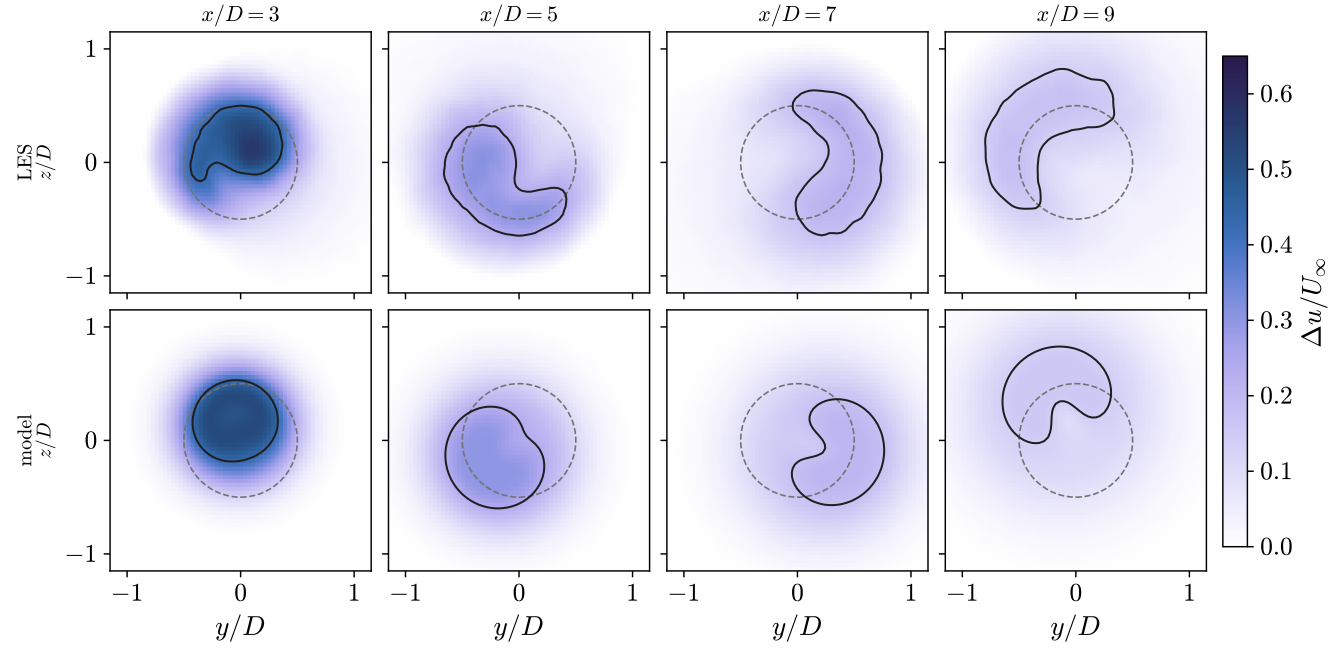
5 Case study: integration in the OFF framework

The following section describes the models implementation into the dynamic wind-farm framework OFF Becker et al. (2024), the successor of FLORIDyn Becker et al. (2022), and is applied exemplarily to a three-turbine row. The phase-resolved model

https://doi.org/10.5194/wes-2026-209
Preprint. Discussion started: 17 November 2026
© Author(s) 2026. CC BY 4.0 License.



(a) $\beta = 2°$



(b) $\beta = 4°$

Figure 11. Prediction of the two held-out cases (helix actuation amplitudes $\beta = 2°$ 11a and $\beta = 4°$ 11b) at $\mathrm{St} = 0.28$. The dashed circle represents the rotor. The solid line is an iso-deficit contour at 75% of the peak deficit of that station, drawn at the same absolute level for LES and model so the traced shapes are directly comparable.

https://doi.org/10.5194/wes-2026-209
Preprint. Discussion started: 17 November 2026
© Author(s) 2026. CC BY 4.0 License.



eawe european academy of wind energy
Open Access WIND ENERGY SCIENCE DISCUSSIONS

Table 3. Calibrated coefficients of the assembled model (rounded to three decimals). Each streamwise-function coefficient is expressed as a function of the pitch amplitude β (in degrees) through the baseline-plus-contribution form of Eq. (16); Γ and r_h vanish at $\beta = 0$ and therefore reduce to pure power laws. The lower block lists the quantities held fixed across all cases.

Function	Coeff.	Amplitude relation $c(\beta)$
$\sigma(k)$, Eq. (10)	b	$0.057 + 0.005\,\beta^{0.545}$
	e	$0.158 + 0.001\,\beta^{2.106}$
$r_0(k)$, Eq. (11)	b	$0.042 + 0.007\,\beta^{0.366}$
	e	$0.177 - 0.002\,\beta^{2.192}$
$\Gamma(k)$, Eq. (12)	L	$1.854\,\beta^{0.379}$
	a	$0.616 - 0.040\,\beta$
	k_0	$7.450 - 0.539\,\beta$
$r_h(k)$, Eq. (13)	a	$0.014\,\beta^{0.424}$
	c	$0.016\,\beta^{0.668}$
$\varphi_h(k,t)$, Eq. (14)	φ_0	control input
	U_c	$(0.831 + 0.017\,\beta)\,U_\infty$
	τ	$(9.012 + 0.581\,\beta)\,D/U_\infty$
Global constants		
$\sigma(k)$	a_0, c_0, k_σ	$0.080\,D$, 0.30, $0.70\,D$
$r_0(k)$	a_0^r, c_0^r, k_s	$0.12\,D$, 0.22, $2.0\,D$
CVP	r_c, d_v	$0.25\,D$, $0.05\,D$
φ_h	k_u	$2.0\,D$
Thrust	C_T, $\eta(\beta)$	0.87, Eq. (6)

is then used to simulate the dynamic farm response. Optimizing the setpoints against the dynamic model itself is a control problem in its own right and is left to future work.

5.1 Implementation

The flow field is carried by observation points that are released at each rotor and advected downstream, so each turbine reacts to the flow state that actually reaches it rather than to an instantaneously equilibrated farm. The wake itself is evaluated by an engineering model at every time step, and it is at this point that the present model enters.

The implementation uses the new PyWake Pedersen et al. (2023) wake-model interface that OFF exposes. Equation (2) is wrapped as a standard wake-deficit model, which makes the surrounding engineering models (superposition, rotor averaging, and the wind-farm solver) available without modification. Three couplings are specific to the helix. First, the pitch amplitude

https://doi.org/10.5194/wes-2026-209
Preprint. Discussion started: 17 November 2026
© Author(s) 2026. CC BY 4.0 License.

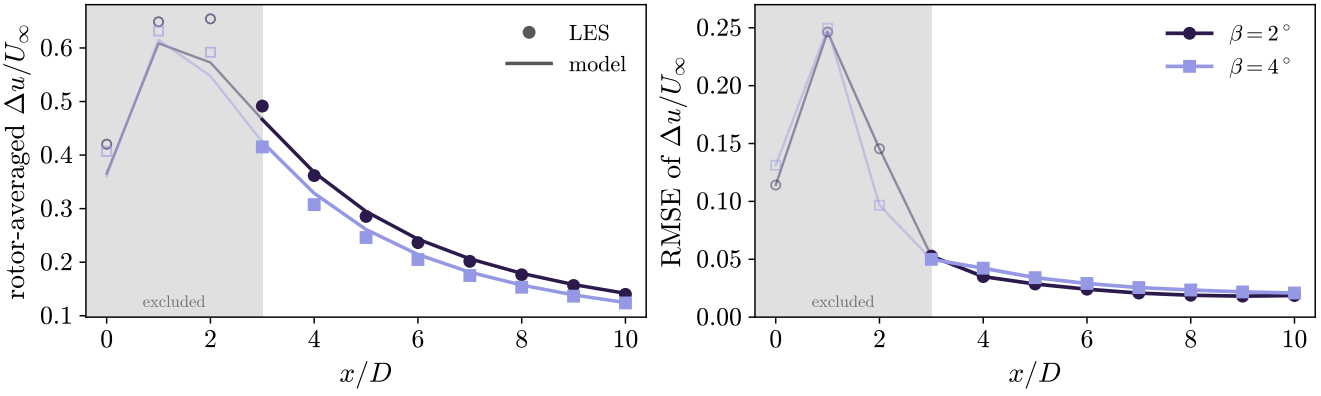


Figure 12. Prediction on the held-out cases over the validity range. (a) Deficit averaged over a rotor disc centered on the wake axis. (b) Per-plane RMSE of the same prediction on the wake mask. The shaded band marks $x/D < 3$, outside the stated validity range;

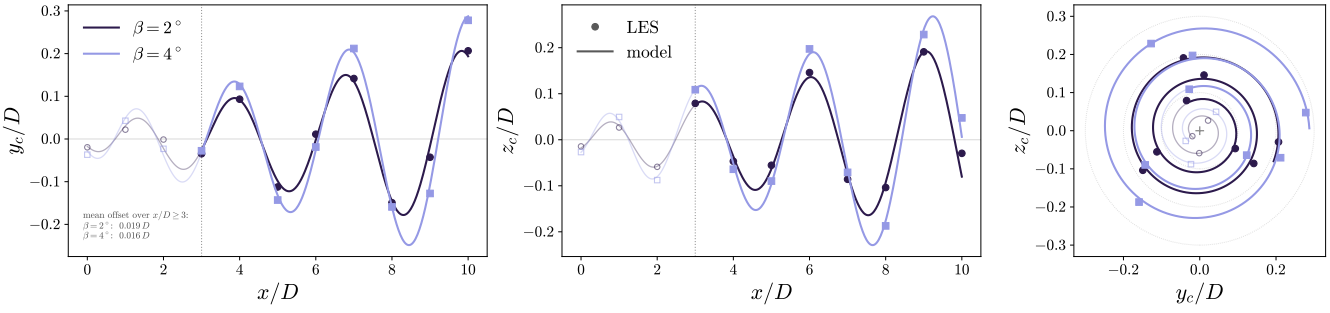


Figure 13. Helical centerline on the held-out cases: (left) top view and (middle) side view; open symbols and the faint line mark $x/D < 3$, outside the stated validity range. (right) The same track viewed along the wake axis, where the centerline appears as the outward spiral; dotted circles are $r_h = 0.1$, 0.2 and $0.3\,D$.

β is carried as an additional per-turbine input alongside the yaw angle, so that each turbine can be actuated independently, and the amplitude-dependent thrust reduction $C_T^{\text{eff}}(\beta)$ from Table 1 is applied to the actuated rotor. Second, the deficit depends on the simulation time. The solver passes the current time t to the model before each evaluation, which fixes the helix phase through Eq. (14), so that the wake a downstream rotor sees is the instantaneous one, at the phase that has convected to it. Third, the actuation phase offset φ_0 of each turbine is carried as a turbine state, alongside the yaw angle and the pitch amplitude; therefore, it travels downstream with the observation points. The offset is constant per turbine here, but it is the quantity a phase-synchronizing controller would act on, and carrying it as a state lays the groundwork for future work in which the model is adapted for that purpose.

Wakes are superposed linearly and sampled over the downstream rotor with a nine-point Gauss integration Abramowitz and Stegun (1970), which matters here because the helix deficit is annular and rotating rather than axisymmetric. No wake-

https://doi.org/10.5194/wes-2026-209
Preprint. Discussion started: 17 November 2026
© Author(s) 2026. CC BY 4.0 License.

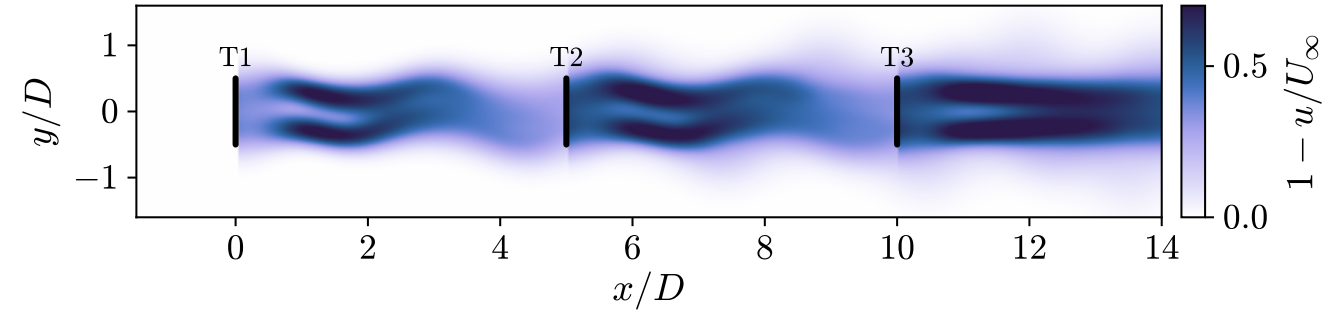


Figure 14. Instantaneous hub-height velocity deficit of the three-turbine row with both upstream turbines actuated at $\beta = 2.5°$. The helical wakes of T1 and T2, and their superposition on T3, are resolved in phase.

deflection or added-turbulence model is used. The case actuates the helix only, and the model carries its own recovery from the calibration. This implies that the farm power gains of this demonstration should not be seen as realistic gains of such a setup, but rather demonstrate the the dynamic response of the model itself.

5.2 Farm and setpoint design

The farm consists of three IEA 22 MW turbines at $5\,D$ spacing (Fig. 14). The ambient wind speed is set as $U_\infty = 8\,\mathrm{m\,s^{-1}}$ with a shear coefficient of $\alpha = 0.12$ and no veer. The helix is operated at the calibration Strouhal number $\mathrm{St} = 0.28$, giving a period $T_e = 127\,\mathrm{s}$. OFF is run with a time step of $4\,\mathrm{s}$, which samples the helix period about thirty times, and with 200 observation points per turbine, so the chains span the $10\,D$ row with margin.

The row starts at a wind direction of $wd = 250°$. Between 600 and $1000\,\mathrm{s}$ the direction turns to 270° at $0.05°\,\mathrm{s^{-1}}$, bringing the row into full alignment, and the helix is switched on at $1800\,\mathrm{s}$ once the farm has settled in its waked state.

5.3 Dynamic response

Figure 15 shows the result of the run. Both transients propagate through the farm at the convection velocity. As the row turns into alignment the farm drops from 28.36 to 14.61 MW, a loss of 48.5%. The farm takes $355\,\mathrm{s}$ beyond the end of the wind direction change to arrive at its new waked state. The rotors are not reacting to the wind direction itself but to the wake that the direction change has since produced upstream of them. Switching the helix on recovers part of that loss, and does so with the same delay. The farm returns to 16.83 MW, a gain of 15.2% over the waked baseline. The rise again arrives in two steps, at 178 and $355\,\mathrm{s}$ after the actuation, and the split across the row is strongly asymmetric: the actuated rotors give up 1.5% of their own power, while T2 gains 35.6% and T3, which sees two mixed wakes in series, gains 60.9%. The thrust and power penalty on the actuated rotors is immediate, whereas the benefit is still in transit, so the farm power sits 1.3% below the greedy level for $172\,\mathrm{s}$. The settled state also carries a time-dependent periodic modulation of the downstream power gain at the actuation frequency, 0.6% peak-to-peak on T2 and 0.7% on T3, caused by the combination of the set wind shear of $\alpha = 0.12$ in the underlaying

https://doi.org/10.5194/wes-2026-209
Preprint. Discussion started: 17 November 2026
© Author(s) 2026. CC BY 4.0 License.

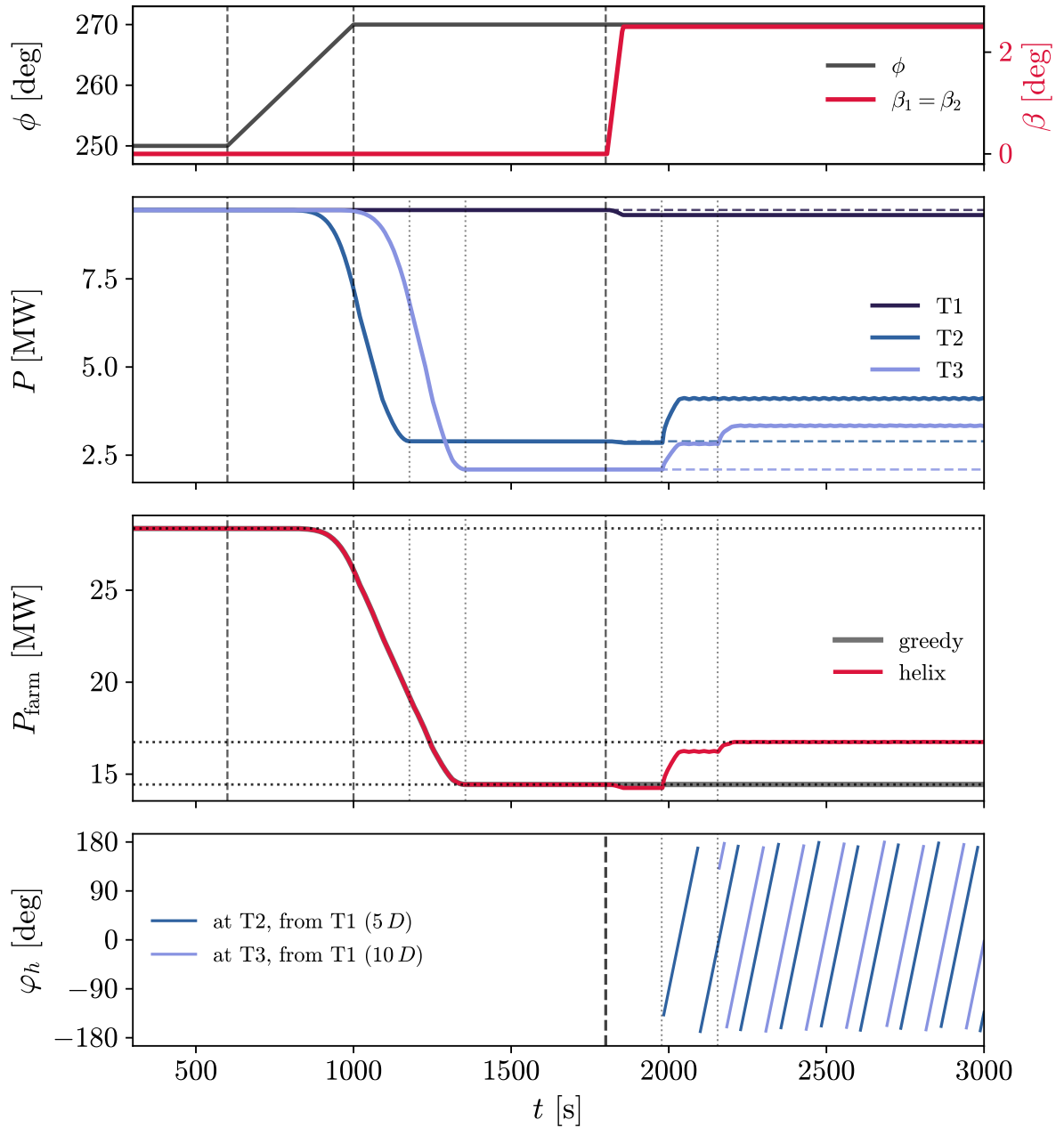


Figure 15. The row through the three states. Dashed verticals mark the direction ramp and the helix step; dotted verticals mark the convection times $5D/U_\infty = 178\,\text{s}$ and $10D/U_\infty = 355\,\text{s}$ after each of them. First panel: ambient wind direction and prescribed actuation amplitude. Second panel: per-turbine power, greedy dashed. Third panel: farm power, with the steady-state (settled) design level of each state (dotted). Fourth panel: Incoming predicted helix phases of T1 measured at T2 and T3. The greedy and helix runs are identical until the helix step.

https://doi.org/10.5194/wes-2026-209
Preprint. Discussion started: 17 November 2026
© Author(s) 2026. CC BY 4.0 License.



eawe european academy of wind energy
Open Access WIND ENERGY SCIENCE DISCUSSIONS

PyWake wind farm site. The figure also shows the arriving helix phase of T1 at T2 and T3 in the fourth panel. This feature of the model can be used for future work, when the model has been adjusted to account for helix phase synchronization.

5.4 Computational cost

The model is analytical, and the cost of using it is correspondingly small. Evaluating the deficit on a 64×64 plane takes 0.15 ms on a single CPU, so a single wake plane costs about 36 ns per point. Inside OFF, one time step of the three-turbine farm takes 21 ms, so the 3000 s simulation shown here runs in 16 s of wall-clock time on a single core, some 190 times faster than real time. This allows for real-time execution and makes the model suitable for application in a closed-loop wind farm controller.

6 Conclusions

This study developed a dynamic engineering wake model for wind turbines under helix actuation, resolving the phase-locked, three-dimensional structure of the actuated wake. Based on observations from phase-averaged actuator-line LES of the IEA 22 MW reference wind turbine, the model combines a momentum-based double-Gaussian ring profile with a Lamb–Oseen displacement field representing the CVP and a parameterized helical centerline. Every wake-plane parameter is expressed as a streamwise function anchored at the rotor plane, and each of these is in turn expressed as a function of the control inputs through baseline-plus-contribution scaling relations of the form $c(\beta) = c_{\text{base}} + c_1 \beta^{c_2}$, so that the model reduces exactly to the calibrated greedy baseline at zero actuation. The complete description requires 12 coefficients per operating point and is driven by three control inputs: the pitch amplitude, the actuation frequency, and the actuation phase. A central structural finding is that the actuation frequency does not alter the velocity deficit shape within the studied band ($\text{St} \in \{0.25, 0.28, 0.30\}$), entering only through the rotation rate and the centerline wavelength, so that amplitude-only calibration suffices. The model was validated on two pitch amplitudes withheld from the calibration procedure and showed excellent agreement with the test data.

Lastly, the model was integrated into the dynamic wind-farm framework OFF Becker et al. (2022, 2024) to evaluate helix control on a three-turbine row taken from free-stream operation into full wake alignment and then actuated. Turning the row into alignment results in a power loss of 48.5%, of which helix actuation returns about a sixth at a pitch amplitude of $2.5°$. The case study demonstrates how the model describes the instantaneous power loss at the actuating turbines, while the varying power gain achieved through wake mixing is only seen after the wakes have convected to the downstream rotors. Furthermore, the case study demonstrates how the model can be used to estimate the phase of an incoming helix wake at downstream rotors for helix wake synchronization purposes.

The availability of a phase-resolved engineering model for helix-actuated wakes has significant implications for the design and operation of wind farms employing this control strategy. It makes the timing of helix engagement, accessible to controller design, and it resolves which side of the helix a downstream rotor meets at a given instant — a prerequisite for estimating helix phase synchronization in turbine arrays and for assessing the partial-wake loading that phase-locked structures impose. Combined with its millisecond evaluation cost, these capabilities allow the strategy to be optimized within model-predictive control frameworks rather than evaluated only at settled operating points, contributing to more effective control system development.

https://doi.org/10.5194/wes-2026-209
Preprint. Discussion started: 17 November 2026
© Author(s) 2026. CC BY 4.0 License.



eawe european academy of wind energy
Open Access WIND ENERGY SCIENCE DISCUSSIONS

Author contributions. TD: conceptualisation, methodology, software, validation, investigation, writing – original draft, visualisation. WY: writing – review & editing, conceptualisation, supervision, resources. JWvW: writing – review & editing, conceptualisation, supervision, resources, funding acquisition.

Competing interests. One of the authors is an Associate editor of Wind Energy Science.

Acknowledgements. This work has been supported by the SUDOCO project, which receives the funding from the European Union's Horizon Europe Programme under the grant No. 101122256.

The authors acknowledge the use of computational resources of the DelftBlue supercomputer, provided by Delft High Performance Computing Centre (https://www.tudelft.nl/dhpc).

https://doi.org/10.5194/wes-2026-209
Preprint. Discussion started: 17 November 2026
© Author(s) 2026. CC BY 4.0 License.



eawe european academy of wind energy
Open Access WIND ENERGY SCIENCE DISCUSSIONS

References

Abbas, N. J., Zalkind, D. S., Pao, L., and Wright, A.: A reference open-source controller for fixed and floating offshore wind turbines, Wind Energy Science, 7, 53–73, https://doi.org/10.5194/wes-7-53-2022, 2022.

Abramowitz, M. and Stegun, I.: Handbook of Mathematical Functions pover, New York, 1970.

Ainslie, J. F.: Calculating the flowfield in the wake of wind turbines, Journal of Wind Engineering and Industrial Aerodynamics, 27, 213–224, https://doi.org/10.1016/0167-6105(88)90037-2, 1988.

Barthelmie, R. J., Hansen, K., Frandsen, S. T., Rathmann, O., Schepers, J. G., Schlez, W., Phillips, J., Rados, K., Zervos, A., Politis, E. S., and Chaviaropoulos, P. K.: Modelling and measuring flow and wind turbine wakes in large wind farms offshore, Wind Energy, 12, 431–444, https://doi.org/10.1002/we.348, 2009.

Bastankhah, M. and Porté-Agel, F.: A new analytical model for wind-turbine wakes, Renewable Energy, 70, 116–123, https://doi.org/10.1016/j.renene.2014.01.002, 2014.

Bastankhah, M. and Porté-Agel, F.: Experimental and theoretical study of wind turbine wakes in yawed conditions, Journal of Fluid Mechanics, 806, 506–541, https://doi.org/10.1017/jfm.2016.595, 2016.

Bastankhah, M., Shapiro, C. R., Shamsoddin, S., Gayme, D. F., and Meneveau, C.: A vortex sheet based analytical model of the curled wake behind yawed wind turbines, Journal of Fluid Mechanics, 933, A2, https://doi.org/10.1017/jfm.2021.1010, 2022.

Becker, M., Ritter, B., Doekemeijer, B., van der Hoek, D., Konigorski, U., Allaerts, D., and van Wingerden, J.-W.: The revised FLORIDyn model: implementation of heterogeneous flow and the Gaussian wake, Wind Energy Science, 7, 2163–2179, https://doi.org/10.5194/wes-7-2163-2022, 2022.

Becker, M., Allaerts, D., and van Wingerden, J.-W.: Ensemble-based flow field estimation using the dynamic wind farm model OFF, Journal of Physics: Conference Series, 2767, 032 083, https://doi.org/10.1088/1742-6596/2767/3/032083, 2024.

Bossanyi, E. A.: Individual blade pitch control for load reduction, Wind Energy, 6, 119–128, https://doi.org/10.1002/we.76, 2003.

Brown, K., Houck, D., Maniaci, D., Westergaard, C., and Kelley, C.: Accelerated wind-turbine wake recovery through actuation of the tip-vortex instability, AIAA Journal, 60, 3298–3310, https://doi.org/10.2514/1.J060772, 2022.

Cheung, L. C., Brown, K. A., Houck, D. R., and deVelder, N. B.: Fluid-dynamic mechanisms underlying wind turbine wake control with Strouhal-timed actuation, Energies, 17, 865, https://doi.org/10.3390/en17040865, 2024.

Churchfield, M. J., Lee, S., Michalakes, J., and Moriarty, P. J.: A numerical study of the effects of atmospheric and wake turbulence on wind turbine dynamics, Journal of Turbulence, 13, N14, https://doi.org/10.1080/14685248.2012.668191, 2012.

Crespo, A., Hernández, J., and Frandsen, S.: Survey of modelling methods for wind turbine wakes and wind farms, Wind Energy, 2, 1–24, https://doi.org/10.1002/(SICI)1099-1824(199901/03)2:1<1::AID-WE16>3.0.CO;2-7, 1999.

Dammann, T., van der Hoek, D., Yu, W., and van Wingerden, J.-W.: Enhanced Wind Farm Performance via Active Wake Control: A Steady-State Approach, in: 2025 American Control Conference (ACC), pp. 2856–2861, https://doi.org/10.23919/acc63710.2025.11107695, 2025.

Dammann, T., van der Hoek, D., Yu, W., and van Wingerden, J.-W.: A novel engineering wake model for helix-actuated wind turbine wakes, Applied Energy, 414, 127 808, https://doi.org/10.1016/j.apenergy.2026.127808, vERIFY co-author list and DOI against the published record, 2026a.

Dammann, T., Yu, W., and van Wingerden, J.-W.: Balancing Actuation Penalties and Wake Recovery: The Efficacy of the Helix in Turbulent Inflows, in: Journal of Physics: Conference Series, vol. 3224, p. 032002, IOP Publishing, 2026b.

https://doi.org/10.5194/wes-2026-209
Preprint. Discussion started: 17 November 2026
© Author(s) 2026. CC BY 4.0 License.



Doekemeijer, B. M., van der Hoek, D., and van Wingerden, J.-W.: Closed-loop model-based wind farm control using FLORIS under time-varying inflow conditions, Renewable Energy, 156, 719–730, https://doi.org/10.1016/j.renene.2020.04.007, 2020.

Fleming, P., King, J., Dykes, K., Simley, E., Roadman, J., Scholbrock, A., Murphy, P., Lundquist, J. K., Moriarty, P., Fleming, K., van Dam, J., Bay, C., Mudafort, R., Lopez, H., Skopek, J., Scott, M., Ryan, B., Guernsey, C., and Brake, D.: Initial results from a field campaign of wake steering applied at a commercial wind farm – Part 1, Wind Energy Science, 4, 273–285, https://doi.org/10.5194/wes-4-273-2019, 2019.

Frederik, J. A. and van Wingerden, J.-W.: On the load impact of dynamic wind farm wake mixing strategies, Renewable Energy, 194, 582–595, https://doi.org/10.1016/j.renene.2022.05.110, 2022.

Frederik, J. A., Doekemeijer, B. M., Mulders, S. P., and van Wingerden, J.-W.: The helix approach: Using dynamic individual pitch control to enhance wake mixing in wind farms, Wind Energy, 23, 1739–1751, https://doi.org/10.1002/we.2513, 2020a.

Frederik, J. A., Weber, R., Cacciola, S., Campagnolo, F., Croce, A., Bottasso, C., and van Wingerden, J.-W.: Periodic dynamic induction control of wind farms: proving the potential in simulations and wind tunnel experiments, Wind Energy Science, 5, 245–257, https://doi.org/10.5194/wes-5-245-2020, 2020b.

Gebraad, P. M. O. and van Wingerden, J.-W.: A control-oriented dynamic model for wakes in wind plants, Journal of Physics: Conference Series, 524, 012 186, https://doi.org/10.1088/1742-6596/524/1/012186, 2014.

Gebraad, P. M. O., Teeuwisse, F. W., van Wingerden, J.-W., Fleming, P. A., Ruben, S. D., Marden, J. R., and Pao, L. Y.: Wind plant power optimization through yaw control using a parametric model for wake effects—a CFD simulation study, Wind Energy, 19, 95–114, https://doi.org/10.1002/we.1822, 2016.

Göçmen, T., van der Laan, P., Réthoré, P.-E., Peña Diaz, A., Larsen, G. C., and Ott, S.: Wind turbine wake models developed at the Technical University of Denmark: A review, Renewable and Sustainable Energy Reviews, 60, 752–769, https://doi.org/10.1016/j.rser.2016.01.113, 2016.

Goit, J. P. and Meyers, J.: Optimal control of energy extraction in wind-farm boundary layers, Journal of Fluid Mechanics, 768, 5–50, https://doi.org/10.1017/jfm.2015.70, 2015.

Gutknecht, J., Becker, M., Muscari, C., Lutz, T., and van Wingerden, J.-W.: Scaling DMD modes for modeling the Helix approach in a lattice-Boltzmann code, Journal of Physics: Conference Series, 2505, 012 040, https://doi.org/10.1088/1742-6596/2505/1/012040, 2023.

Gutknecht, J., Krause, J., Bottasso, C. L., and van Wingerden, J.-W.: A vortex-based wake model for helix active wake control, Journal of Physics: Conference Series, 3224, 032 060, https://doi.org/10.1088/1742-6596/3224/3/032060, the Science of Making Torque from Wind (TORQUE 2026), 2026.

Houck, D. R.: Review of wake management techniques for wind turbines, Wind Energy, 25, 195–220, https://doi.org/10.1002/we.2668, 2022.

Howland, M. F., Bossuyt, J., Martínez-Tossas, L. A., Meyers, J., and Dabiri, J. O.: Wake structure in actuator disk models of wind turbines in yaw under uniform inflow conditions, Journal of Renewable and Sustainable Energy, 8, 043 301, https://doi.org/10.1063/1.4955091, 2016.

Howland, M. F., Lele, S. K., and Dabiri, J. O.: Wind farm power optimization through wake steering, Proceedings of the National Academy of Sciences, 116, 14 495–14 500, https://doi.org/10.1073/pnas.1903680116, 2019.

Ishihara, T. and Qian, G.-W.: A new Gaussian-based analytical wake model for wind turbines considering ambient turbulence intensities and thrust coefficient effects, Journal of Wind Engineering and Industrial Aerodynamics, 177, 275–292, https://doi.org/10.1016/j.jweia.2018.04.010, 2018.

Ivanell, S., Mikkelsen, R., Sørensen, J. N., and Henningson, D.: Stability analysis of the tip vortices of a wind turbine, Wind Energy, 13, 705–715, https://doi.org/10.1002/we.391, 2010.

https://doi.org/10.5194/wes-2026-209
Preprint. Discussion started: 17 November 2026
© Author(s) 2026. CC BY 4.0 License.

Jensen, N. O.: A note on wind generator interaction, Tech. Rep. Risø-M-2411, Risø National Laboratory, Roskilde, Denmark, 1983.

Jonkman, B. J.: TurbSim user's guide: Version 1.50, Tech. Rep. NREL/TP-500-46198, National Renewable Energy Laboratory, Golden, CO, USA, 2009.

Katić, I., Højstrup, J., and Jensen, N. O.: A simple model for cluster efficiency, in: Proceedings of the European Wind Energy Association Conference and Exhibition (EWEC'86), pp. 407–410, Rome, Italy, 1986.

Keane, A.: Advancement of an analytical double-Gaussian full wind turbine wake model, Renewable Energy, 171, 687–708, https://doi.org/10.1016/j.renene.2021.02.078, 2021.

Keane, A., Aguirre, P. E. O., Ferchland, H., Clive, P., and Gallacher, D.: An analytical model for a full wind turbine wake, Journal of Physics: Conference Series, 753, 032 039, https://doi.org/10.1088/1742-6596/753/3/032039, 2016.

Korb, H., Asmuth, H., and Ivanell, S.: The characteristics of helically deflected wind turbine wakes, Journal of Fluid Mechanics, 965, A2, https://doi.org/10.1017/jfm.2023.390, 2023.

Larsen, G. C., Madsen, H. A., Thomsen, K., and Larsen, T. J.: Wake meandering: a pragmatic approach, Wind Energy, 11, 377–395, https://doi.org/10.1002/we.267, 2008.

Lejeune, M., Moens, M., and Chatelain, P.: A meandering-capturing wake model coupled to rotor-based flow-sensing for operational wind farm flow prediction, Frontiers in Energy Research, 10, 884 068, https://doi.org/10.3389/fenrg.2022.884068, 2022.

Lignarolo, L. E. M., Ragni, D., Scarano, F., Simão Ferreira, C. J., and van Bussel, G. J. W.: Tip-vortex instability and turbulent mixing in wind-turbine wakes, Journal of Fluid Mechanics, 781, 467–493, https://doi.org/10.1017/jfm.2015.470, 2015.

Mao, X. and Sørensen, J. N.: Far-wake meandering induced by atmospheric eddies in flow past a wind turbine, Journal of Fluid Mechanics, 846, 190–209, https://doi.org/10.1017/jfm.2018.275, 2018.

Martínez-Tossas, L. A., Churchfield, M. J., and Meneveau, C.: Optimal smoothing length scale for actuator line models of wind turbine blades based on Gaussian body force distribution, Wind Energy, 20, 1083–1096, https://doi.org/10.1002/we.2081, 2017.

Martínez-Tossas, L. A., Annoni, J., Fleming, P. A., and Churchfield, M. J.: The aerodynamics of the curled wake: a simplified model for skewed wakes, Wind Energy Science, 4, 127–138, https://doi.org/10.5194/wes-4-127-2019, 2019.

Medici, D. and Alfredsson, P. H.: Measurements on a wind turbine wake: 3D effects and bluff body vortex shedding, Wind Energy, 9, 219–236, https://doi.org/10.1002/we.156, 2006.

Meyers, J., Bottasso, C., Dykes, K., Fleming, P., Gebraad, P., Giebel, G., Göçmen, T., and van Wingerden, J.-W.: Wind farm flow control: prospects and challenges, Wind Energy Science, 7, 2271–2306, https://doi.org/10.5194/wes-7-2271-2022, 2022.

Munters, W. and Meyers, J.: An optimal control framework for dynamic induction control of wind farms and their interaction with the atmospheric boundary layer, Philosophical Transactions of the Royal Society A, 375, 20160 100, https://doi.org/10.1098/rsta.2016.0100, 2017.

Munters, W. and Meyers, J.: Towards practical dynamic induction control of wind farms: analysis of optimally controlled wind-farm boundary layers and sinusoidal induction control of first-row turbines, Wind Energy Science, 3, 409–425, https://doi.org/10.5194/wes-3-409-2018, 2018.

Muscari, C., Schito, P., Viré, A., Zasso, A., van der Hoek, D., and van Wingerden, J.-W.: Physics informed DMD for periodic dynamic induction control of wind farms, Journal of Physics: Conference Series, 2265, 022 057, https://doi.org/10.1088/1742-6596/2265/2/022057, 2022.

National Renewable Energy Laboratory: OpenFAST documentation, https://github.com/OpenFAST/openfast, version 3.5, 2024.

https://doi.org/10.5194/wes-2026-209
Preprint. Discussion started: 17 November 2026
© Author(s) 2026. CC BY 4.0 License.

Niayifar, A. and Porté-Agel, F.: Analytical modeling of wind farms: A new approach for power prediction, Energies, 9, 741, https://doi.org/10.3390/en9090741, 2016.

Okulov, V. L. and Sørensen, J. N.: Stability of helical tip vortices in a rotor far wake, Journal of Fluid Mechanics, 576, 1–25, https://doi.org/10.1017/S0022112006004228, 2007.

Pedersen, M. M., van der Laan, P., Friis-Møller, M., Forsting, A. M., Rinker, J., and Réthoré, P.-E.: PyWake: An open-source wind farm simulation tool, https://doi.org/10.5281/zenodo.2562662, 2023.

Porté-Agel, F., Bastankhah, M., and Shamsoddin, S.: Wind-turbine and wind-farm flows: A review, Boundary-Layer Meteorology, 174, 1–59, https://doi.org/10.1007/s10546-019-00473-0, 2020.

Qian, G.-W. and Ishihara, T.: A novel double-Gaussian full wake model for wind turbines considering dependence on thrust coefficient and ambient turbulence intensity, Applied Energy, 391, 125 859, https://doi.org/10.1016/j.apenergy.2025.125859, 2025.

Sanderse, B., van der Pijl, S. P., and Koren, B.: Review of computational fluid dynamics for wind turbine wake aerodynamics, Wind Energy, 14, 799–819, https://doi.org/10.1002/we.458, 2011.

Schreiber, J., Balbaa, A., and Bottasso, C. L.: Brief communication: A double-Gaussian wake model, Wind Energy Science, 5, 237–244, https://doi.org/10.5194/wes-5-237-2020, 2020.

Shapiro, C. R., Gayme, D. F., and Meneveau, C.: Modelling yawed wind turbine wakes: a lifting line approach, Journal of Fluid Mechanics, 841, R1, https://doi.org/10.1017/jfm.2018.75, 2018.

Sharma, A., Brazell, M. J., Vijayakumar, G., Ananthan, S., Cheung, L., deVelder, N., Henry de Frahan, M. T., Matula, N., Mullowney, P., Rood, J., Sakievich, P., Almgren, A., Crozier, P. S., and Sprague, M. A.: ExaWind: Open-source CFD for hybrid-RANS/LES geometry-resolved wind turbine simulations in atmospheric flows, Wind Energy, 27, 225–257, https://doi.org/10.1002/we.2886, 2024.

Smagorinsky, J.: General circulation experiments with the primitive equations: I. The basic experiment, Monthly Weather Review, 91, 99–164, https://doi.org/10.1175/1520-0493(1963)091<0099:GCEWTP>2.3.CO;2, 1963.

Sørensen, J. N. and Shen, W. Z.: Numerical modeling of wind turbine wakes, Journal of Fluids Engineering, 124, 393–399, https://doi.org/10.1115/1.1471361, 2002.

Sprague, M. A., Ananthan, S., Vijayakumar, G., and Robinson, M.: ExaWind: A multifidelity modeling and simulation environment for wind energy, Journal of Physics: Conference Series, 1452, 012 071, https://doi.org/10.1088/1742-6596/1452/1/012071, 2020.

Stevens, R. J. A. M. and Meneveau, C.: Flow structure and turbulence in wind farms, Annual Review of Fluid Mechanics, 49, 311–339, https://doi.org/10.1146/annurev-fluid-010816-060206, 2017.

Taschner, E., van Vondelen, A. A. W., Verzijlbergh, R., and van Wingerden, J.-W.: On the performance of the helix wind farm control approach in the conventionally neutral atmospheric boundary layer, Journal of Physics: Conference Series, 2505, 012 006, https://doi.org/10.1088/1742-6596/2505/1/012006, 2023.

Taschner, E., Folkersma, M., Martínez-Tossas, L. A., Verzijlbergh, R., and van Wingerden, J.-W.: A new coupling of a GPU-resident large-eddy simulation code with a multiphysics wind turbine simulation tool, Wind Energy, 27, 1152–1172, https://doi.org/10.1002/we.2844, 2024.

Troldborg, N., Sørensen, J. N., and Mikkelsen, R.: Numerical simulations of wake characteristics of a wind turbine in uniform inflow, Wind Energy, 13, 86–99, https://doi.org/10.1002/we.345, 2010.

van den Berg, D., de Tavernier, D., and van Wingerden, J.-W.: Using the helix mixing approach on floating offshore wind turbines, Journal of Physics: Conference Series, 2265, 042 011, https://doi.org/10.1088/1742-6596/2265/4/042011, 2022.

https://doi.org/10.5194/wes-2026-209
Preprint. Discussion started: 17 November 2026
© Author(s) 2026. CC BY 4.0 License.

van den Berg, D., de Tavernier, D., and van Wingerden, J.-W.: The dynamic coupling between the pulse wake mixing strategy and floating wind turbines, Wind Energy Science, 8, 849–864, https://doi.org/10.5194/wes-8-849-2023, 2023.

van den Broek, M. J., De Tavernier, D., Sanderse, B., and van Wingerden, J.-W.: Adjoint optimisation for wind farm flow control with a free-vortex wake model, Renewable Energy, 201, 944–953, https://doi.org/10.1016/j.renene.2022.10.120, 2022.

van der Hoek, D., Frederik, J., Huang, M., Scarano, F., Simão Ferreira, C., and van Wingerden, J.-W.: Experimental analysis of the effect of dynamic induction control on a wind turbine wake, Wind Energy Science, 7, 1305–1320, https://doi.org/10.5194/wes-7-1305-2022, 2022.

van der Hoek, D., van den Abbeele, B., Simão Ferreira, C., and van Wingerden, J.-W.: Maximizing wind farm power output with the helix approach: Experimental validation and wake analysis using tomographic particle image velocimetry, Wind Energy, 27, 463–482, https://doi.org/10.1002/we.2896, 2024.

van Vondelen, A. A. W., Navalkar, S. T., Kerssemakers, D. R. H., and van Wingerden, J.-W.: Enhanced wake mixing in wind farms using the Helix approach: A loads sensitivity study, in: Proceedings of the 2023 American Control Conference (ACC), pp. 831–836, San Diego, CA, USA, https://doi.org/10.23919/ACC55779.2023.10155965, 2023a.

van Vondelen, A. A. W., Ottenheym, J., Pamososuryo, A. K., Navalkar, S. T., and van Wingerden, J.-W.: Phase synchronization for helix enhanced wake mixing in downstream wind turbines, IFAC-PapersOnLine, 56, 8426–8431, https://doi.org/10.1016/j.ifacol.2023.10.1039, 2023b.

Vermeer, L. J., Sørensen, J. N., and Crespo, A.: Wind turbine wake aerodynamics, Progress in Aerospace Sciences, 39, 467–510, https://doi.org/10.1016/S0376-0421(03)00078-2, 2003.

Yılmaz, A. O. and Meyers, J.: Optimal dynamic induction control of a pair of inline wind turbines, Physics of Fluids, 30, 085 106, https://doi.org/10.1063/1.5038600, 2018.

Zahle, F., Barlas, T., Lønbæk, K., Bortolotti, P., Zalkind, D., Wang, L., Labuschagne, C., Sethuraman, L., and Barter, G.: Definition of the IEA Wind 22-Megawatt Offshore Reference Wind Turbine, Tech. Rep. DTU Wind Report E-0243, Technical University of Denmark, International Energy Agency Wind TCP Task 55, https://doi.org/10.11581/DTU.00000317, 2024.

Zong, H. and Porté-Agel, F.: A point vortex transportation model for yawed wind turbine wakes, Journal of Fluid Mechanics, 890, A8, https://doi.org/10.1017/jfm.2020.123, 2020.